BRAIN
ORIGINAL ARTICLE

RNF213 loss-of-function promotes pathological angiogenesis in moyamoya disease via the Hippo pathway

Fei Ye,[1,2,†] Xingyang Niu,[1,†] Feng Liang,[3,†] Yuanyuan Dai,[1,4] Jie Liang,[1] Jiaoxing Li,[1,5] Xiaoxin Wu,[1] Hanyue Zheng,[1] Tiewei Qi[3] and Wenli Sheng[1,5]

[†]These authors contributed equally to this work.

Moyamoya disease is an uncommon cerebrovascular disorder characterized by steno-occlusive changes in the circle of Willis and abnormal vascular network development. Ring finger protein 213 (*RNF213*) has been identified as an important susceptibility gene for Asian patients, but researchers have not completely elucidated whether *RNF213* mutations affect the pathogenesis of moyamoya disease.

Using donor superficial temporal artery samples, whole-genome sequencing was performed to identify *RNF213* mutation types in patients with moyamoya disease, and histopathology was performed to compare morphological differences between patients with moyamoya disease and intracranial aneurysm. The vascular phenotype of *RNF213*-deficient mice and zebrafish was explored *in vivo*, and *RNF213* knockdown in human brain microvascular endothelial cells was employed to analyse cell proliferation, migration and tube formation abilities *in vitro*. After bioinformatics analysis of both cell and bulk RNA-seq data, potential signalling pathways were measured in *RNF213*-knockdown or *RNF213*-knockout endothelial cells.

We found that patients with moyamoya disease carried pathogenic mutations of *RNF213* that were positively associated with moyamoya disease histopathology. *RNF213* deletion exacerbated pathological angiogenesis in the cortex and retina. Reduced *RNF213* expression led to increased endothelial cell proliferation, migration and tube formation. Endothelial knockdown of *RNF213* activated the Hippo pathway effector Yes-associated protein (*YAP*)/tafazzin (*TAZ*) and promoted the overexpression of the downstream effector *VEGFR2*. Additionally, inhibition of *YAP*/*TAZ* resulted in altered cellular *VEGFR2* distribution due to defects in trafficking from the Golgi apparatus to the plasma membrane and reversed *RNF213* knockdown-induced angiogenesis. All these key molecules were validated in ECs isolated from *RNF213*-deficient animals.

Our findings may suggest that loss-of-function of *RNF213* mediates the pathogenesis of moyamoya disease via the Hippo pathway.

1 Department of Neurology, The First Affiliated Hospital, Sun Yat-sen University, Guangzhou 510080, China
2 Department of Neurosurgery, Southwest Hospital, Third Military Medical University (Army Medical University), Chongqing 400038, China
3 Department of Neurosurgery, The First Affiliated Hospital, Sun Yat-sen University, Guangzhou 510080, China
4 Department of Neurology, The Seventh Affiliated Hospital, Sun Yat-sen University, Shenzhen 517108, China
5 Guangdong Provincial Key Laboratory of Diagnosis and Treatment of Major Neurological Diseases, The First Affiliated Hospital, Sun Yat-sen University, Guangzhou 510080, China

Received February 17, 2023. Revised June 01, 2023. Accepted June 18, 2023. Advance access publication July 3, 2023

Correspondence to: Wenli Sheng
Department of Neurology, The First Affiliated Hospital, Sun Yat-sen University
No. 58 Zhongshanerlu Road, Guangzhou, Guangdong 510080, China
E-mail: shengwl@mail.sysu.edu.cn

Correspondence may also be addressed to: Tiewei Qi
Department of Neurosurgery, The First Affiliated Hospital, Sun Yat-sen University
No. 58 Zhongshanerlu Road, Guangzhou, Guangdong 510080, China
E-mail: qitiewei@mail.sysu.edu.cn

Keywords: moyamoya disease; *RNF213*; angiogenesis; hippo pathway

Introduction

Moyamoya disease (MMD) is an uncommon cerebrovascular disorder characterized by progressive stenosis and/or occlusion of the circle of Willis with an abnormally proliferative vascular network at the base of the skull (moyamoya vessels).[1] MMD is a major cause of stroke with a relatively high risk of recurrent cerebrovascular events. This disease exhibits a diverse geographical distribution, with high incidence rates in East Asian countries, and a bimodal age of onset: 5–9 years of age and the middle 40s.[2,3] The pathological hallmarks of MMD have already been reported via a detailed scientific autopsy of intracranial large arteries, while the natural history of moyamoya vessels has been carefully described using the Suzuki staging system.[4–6] However, the aetiology and pathogenesis of MMD are not fully understood.[7] Effective therapeutic strategies to alleviate disease deterioration and reverse disease progression are still lacking.[8] Revascularization surgery is widely used to improve the vascular reserve capacity and prevent further cerebral vascular attacks, but postoperative hyperperfusion syndrome causes poor outcomes.[8] Therefore, elucidation of the molecular mechanism of this disease might identify optimal treatments.

The ring finger protein 213 (*RNF213*) gene on chromosome 17q25.3 has been identified as an important susceptibility gene for MMD.[9,10] RNF213 is a 591 kDa protein with two functional domain structures (a Walker motif and a RING finger domain) with ATPase and ubiquitin ligase catalytic activities. Recent genome-wide association studies (GWASs) have revealed many single-nucleotide polymorphisms (SNPs) at the *RNF213* locus in East Asian patients.[9–15] Of these SNPs, the mutant allele p.R4810K (c.14429G>A, rs112735431) is closely related to MMD and shows a strong genetic effect associated with earlier disease onset and worse outcome.[7] This mutation is common and is present in 95% of patients with familial MMD, 73% of patients with sporadic MMD, and 1.4% of healthy controls.[14] Although controversy persists regarding whether *RNF213* mutations induce a loss-of-function or gain-of-function allele status, accumulating evidence has suggested that missense mutations might disrupt gene transcription and protein function to a certain extent. *RNF213* mutation causes pathological dysregulation of substrate ubiquitination due to changes in the functional domain.[16] In addition, several responsible *RNF213* mutations have been identified in MMD patients through whole-exome sequencing (WES); these mutations include mainly a 21-bp in-frame insertion starting at amino acid 4951, two 3-bp deletions (p.A529del, p.K4115del) and a *de novo* genetic variant (c.11986_11989delCCGTinsGGGTTAG).[15,17] Some patients with MMD might present with *RNF213* loss; thus, the role of these mutations is not clear. In this study, we aimed to determine the functions and underlying mechanisms of pathogenic *RNF213* mutations in patients with MMD.

Materials and methods

A detailed 'Materials and methods' section is provided in the online Supplementary material.

Study approval

Animal experiments were conducted in accordance with the National Institutes of Health Animal Use Guidelines. Informed consent was obtained from every participant. This study was approved by the Ethics Committee for Clinical Research and Animal Trials of the First Affiliated Hospital of Sun Yat-sen University [(2022)330].

Statistical analysis

Values are presented as the means ± standard deviations (SDs). Two-tailed non-parametric tests followed by the Mann–Whitney U-test (for comparisons of two groups) or one-way ANOVA followed by the Kruskal–Wallis test (for comparisons of three or more groups) were used to calculate the statistical significance. A P-value < 0.05 was used to indicate statistically significant differences. All calculations were performed using GraphPad Prism software (v9.0) or R Project for Statistical Computing software (v4.1.2).

Results

Some MMD patients carry loss-of-function *RNF213* mutations

Although only a few common *RNF213* SNPs have been implicated in MMD to date, studies on the types of genetic variations have been informative and have provided clues about the pathogenesis of MMD. Donor superficial temporal arteries (STAs) from six patients with sporadic MMD undergoing direct bypass were used for whole-genome sequencing (WGS). The raw data from each sample were processed and analysed, as shown in Supplementary Fig. 1A. An average of 99.84% of the raw data aligned to the human reference genome. After 5.68% of duplicate reads were removed, the mean sequencing depth was 33.86×, and the sequencing coverage of the target region was 99.36% (Supplementary Fig. 1B and Supplementary Table 1).

First, variants with a frequency <1% in national reference databases, particularly the 1000 Genomes Project, the Single Nucleotide Polymorphism Database, and the Database of Genomic Variants (DGV), were retained. Next, variants located in the coding region or around the splicing site were retained. Ultimately, we focused

principally on *RNF213* variants. Except for reported missense and silent SNPs, no insertion/deletion (InDel) or structural variant (SV) of the *RNF213* gene was detected in this study. However, we identified a homozygous deletion of the copy number variant (CNV) in the *RNF213* coding sequence in two sporadic cases (33.33%) that might impair the transcription of exon 3 and exon 16 in the gene (Fig. 1A and Supplementary Table 2). Furthermore, the clinical significance of both CNVs was determined according to practical guidelines.[18] One CNV deletion (GRch37: chr17:78287302-78291400 or GRCh38: chr17:80317600-80313502) was a benign CNV because of three similar records in the DGV. Another newly discovered CNV deletion (GRch37: chr17:78247202-78252500 or GRCh38: chr17:80278701-80273403) was compared with a known microduplication syndrome and the clinical features of patients in DECIPHER, a database of genomic variations and phenotypes in humans determined using Ensembl resources. This mutation was matched to not only CNV syndromes but also abnormalities of cardiovascular arteries and a likely pathogenic CNV deletion that was determined to be a clinically relevant CNV.

The sense DNA strand of wild-type *RNF213* was downloaded from the Ensembl database, and 5207 amino acids of the RNF213 protein were obtained from the UniProt database to explore the effect of CNV deletions on RNF213 protein structure and function. The coding sequences of these CNV deletions were translated using ExPASy software. Then, coding sequence alignments between wild-type and CNV deletions showed that the benign CNV deletion only exhibited a very tiny gap (0.58%), but the clinically relevant CNV had a largely different identity from that of wild-type *RNF213* (Supplementary Table 3). The 3D protein structures were automatically predicted using SWISS-MODEL and Phyre2 software. Compared with wild-type RNF213, the benign CNV deletion showed highly similar characteristics, while the clinically relevant CNV showed a completely different protein structure and functional domain (Fig. 1B).

In addition, 44 patients with MMD and 30 patients with intracranial aneurysm (IA) were enrolled in a clinical cohort at our hospital between July 2020 and July 2022. This cohort was used to measure these *RNF213* mutations in peripheral blood DNA samples. The 20 STA DNA samples in MMD patients from this cohort were isolated for validation. Sanger sequencing was performed to determine the pathogenic *RNF213* mutations (p.R4810K mutation, CNV deletion in exon 3) and benign CNV deletion in exon 16. These results revealed that the *RNF213* p.R4810K mutation was more common in MMD patients than in patients with intracranial aneurysm (43.18% versus 33.33%). Neither CNV was observed in intracranial aneurysm patients, but a pathogenic CNV mutation in exon 3 was detected in seven MMD patients (15.91%, all heterozygous), as shown in Supplementary Table 4. Interestingly, only three STA samples (15.00%) contained identical heterozygous mutations, while one (5.00%) presented a homozygous mutation (Supplementary Table 5).

The pathogenic *RNF213* p.R4810K mutation does not affect the RNF213 structure; it is a dominant mutation that deregulates E3 function and decreases overall ubiquitination levels.[16,19,20] Indeed, we isolated the STA proteins from one patient with intracranial aneurysm and one MMD patient with a heterozygous *RNF213* mutation in exon 3. Protein quantification analysis showed significantly reduced *RNF213* and ubiquitin levels (Fig. 1C).

In summary, this study is the first to report a novel CNV deletion in *RNF213* in patients with MMD, suggesting that pathogenic *RNF213* mutations might result in a loss-of-function rather than a gain-of-function in some MMD patients.

Pathogenic *RNF213* mutation promotes intimal hyperplasia

MMD is a proliferative vasculopathy typically characterized by a hyperplastic intima and thin media.[4,7] Therefore, the possible relationship between a common RNF213 pathogenic mutation (p.R4810K) and MMD histopathology was explored in this study. Another set of 18 donor STA samples from MMD patients and 18 STA samples from patients with intracranial aneurysm were compared (Supplementary Table 6).

Haematoxylin and eosin staining was used for a morphometric analysis of the vascular wall structure. No significant differences in artery wall thickness were observed between MMD and intracranial aneurysm patients (251.15 ± 101.76 versus 292.11 ± 63.75 μm, $P = 0.079$). We analysed the ratio of tunica media to artery wall thickness in this study to exclude individual differences in artery size. A marked reduction in tunica media thickness was observed in the MMD samples compared with the intracranial aneurysm samples (Fig. 1F). The vascular smooth muscle fibres were then stained with an antibody against α-smooth muscle actin (α-SMA) using immunohistochemistry (IHC), and the average density of smooth muscle fibres per region of interest (ROI) was automatically analysed using Quantitative Pathology and Bioimage Analysis (QuPath) software (v0.3.0), which indicated a significant loss of smooth muscle in MMD patients compared with patients with intracranial aneurysm (Fig. 1D). However, subgroup analyses revealed that the RNF213 p.R4810K mutation was not associated with thinner smooth muscles in either MMD or intracranial aneurysm patients (Fig. 1F).

Weigert's resorcin-fuchsin staining was used for the morphometric analysis of the internal elastic membranes. The ratio of tunica intima (mainly internal elastic membranes) to artery wall thickness was markedly increased in the MMD samples compared to the intracranial aneurysm samples (Fig. 1G). Interestingly, subgroup analyses revealed that MMD patients carrying the RNF213 mutation (p.R4810K) exhibited significantly thicker internal elastic membrane layers (Fig. 1G). The pathogenic *RNF213* mutation promoted a homogeneous distribution of thicker internal elastic membranes, which was completely different from an eccentric increase due to atherosclerosis.[21] In addition, an ROI-based quantitative analysis of the proliferation marker Ki-67 was performed in the tunica intima and revealed an increased number of Ki-67$^+$ cells in MMD patients carrying the RNF213 p.R4810K mutation (Fig. 1E). Therefore, our findings suggest that the pathogenic *RNF213* mutation induces proliferative changes in the tunica intima and is strongly associated with MMD histopathology.

RNF213 deletion promotes pathological angiogenesis *in vivo*

As a method to observe the vascular phenotype of pathological angiogenesis *in vivo*, we constructed both *Rnf213*-deficient mice (*Rnf213*$^{-/-}$) and *rnf213*-deficient zebrafish (*rnf213*$^{-/-}$) to mimic the loss of *RNF213* function using the CRISPR–Cas9 gene-editing system. The models were confirmed by Sanger sequencing, semiquantitative analyses of mRNA and protein levels, and agarose gel electrophoresis (Fig. 2A). The homozygous mutant mice showed a 151-bp deletion mutation in intron 6 and exon 7 of *Rnf213* at chromosome 11 that caused a 46-bp loss of the coding sequence. The homozygous mutant zebrafish presented with a small deletion of 7 bp in exon 2 of *rnf213* at chromosome 3.

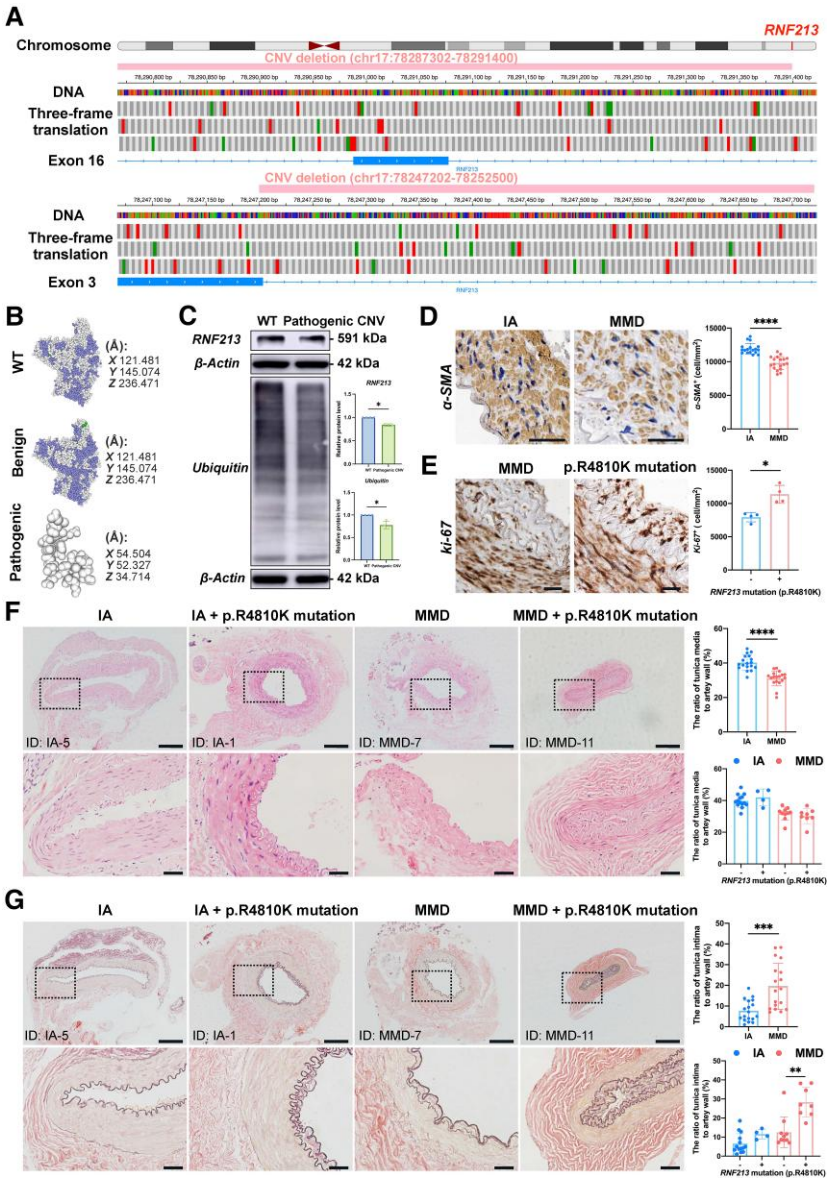

Figure 1 ***RNF213*** **loss-of-function mutations exist in some MMD patients and are positively associated with intimal hyperplasia in MMD patients.** (**A**) The integrative genomics viewer (IGV) application showed a benign copy number variant (CNV) deletion (chr17:78287302-78291400) that completely damages the genomic sequence of exon 3 in *RNF213*. The green boxes indicate a start codon, while the red boxes indicate termination codons in the three-frame translation. (**B**) The protein structure of the wild-type (WT) RNF213 protein (Q63HN8) was modelled with 100.0% confidence based on the single highest-scoring template of the well-known mouse *Rnf213* (c7oikA). The benign CNV deletion of *RNF213* showed a high identity (99.42%) with WT, while the clinically relevant CNV deletion of *RNF213* showed a very low similarity (30.48%) with WT, and only 69 residues were modelled with 43.4% confidence using SWISS-Model and Phyre2. (**C**) Quantitative analysis of RNF213 and ubiquitin protein levels in one intracranial aneurysm (IA) patient and moyamoya disease (MMD) patient carrying the pathogenic *RNF213* mutation of exon 3 (*RNF213*, $n = 4$, 1.00 ± 0.00 versus 0.84 ± 0.03, $P = 0.0286$; ubiquitin, $n = 4$, 1.00 ± 0.00 versus 0.78 ± 0.09, $P = 0.0286$). (**D**) The vascular smooth muscles were then stained with an *α-SMA* antibody, and the region of interest (ROI)-based quantitative analysis of α-SMA$^+$ cells in the tunica media indicated a relative loss of smooth muscle in MMD patients ($n = 18$, 11944.81 ± 783.90 versus 9796.53 ± 962.64 cell/mm^2, $P < 0.0001$). Scale bar = 20 μm. (**E**) The density of *Ki-67* was quantitatively analysed in the tunica intima, which indicated the presence of increased number of *Ki-67*$^+$ cells in MMD patients with *RNF213* mutation ($n = 4$, 7944.90 ± 706.61 versus $11\ 373.69 \pm 1348.96$ cell/mm^2, $P = 0.0286$). Scale bar = 20 μm. (**F**) Haematoxylin and eosin staining was used for morphometric analysis of the vascular wall structure of donor superficial temporal artery (STA) sections from MMD and IA patients. MMD patients showed a significantly thinner tunica media than IA patients ($n = 18$, 31.09 ± 4.35 versus $40.22 \pm 4.33\%$, $P < 0.0001$). No significant difference in tunica media thickness was observed between MMD patients with *RNF213* mutation and those without *RNF213* mutation ($n = 8$ versus 10, 30.19 ± 4.86 versus $31.82 \pm 4.01\%$, $P = 0.3599$). A significant difference in tunica media thickness was not observed between IA patients carrying *RNF213* mutation and those without *RNF213* mutation ($n = 4$ versus 14, 42.00 ± 5.27 versus $39.71 \pm 4.11\%$, $P = 0.4418$). Scale bar = 200 μm (*top*); scale bar = 40 μm (*bottom*). (**G**) Weigert's resorcin-fuchsin staining was applied for morphometric analysis of the internal elastic membranes in MMD and IA patients. MMD patients showed significantly thicker internal elastic membranes than IA patients ($n = 18$, 19.53 ± 11.16 versus $7.68 \pm 5.12\%$, $P = 0.0007$). MMD patients carrying *RNF213* mutation presented with a significantly greater tunica intima thickness than MMD patients without *RNF213* mutation ($n = 8$ versus 10, 28.29 ± 7.87 versus $12.53 \pm 8.02\%$, $P = 0.0014$). No significant difference in tunica intima thickness was observed between IA patients with *RNF213* mutation and those without *RNF213* mutation ($n = 4$ versus 14, 11.55 ± 2.54 versus $6.58 \pm 5.18\%$, $P = 0.0791$). Scale bar = 200 μm (*top*); scale bar = 40 μm (*bottom*). Each dot represents one sample. The means ± SDs are shown. The dashed line indicates the ROI. $^*P < 0.05$, $^{**}P < 0.01$, $^{***}P < 0.001$ and $^{****}P < 0.0001$.

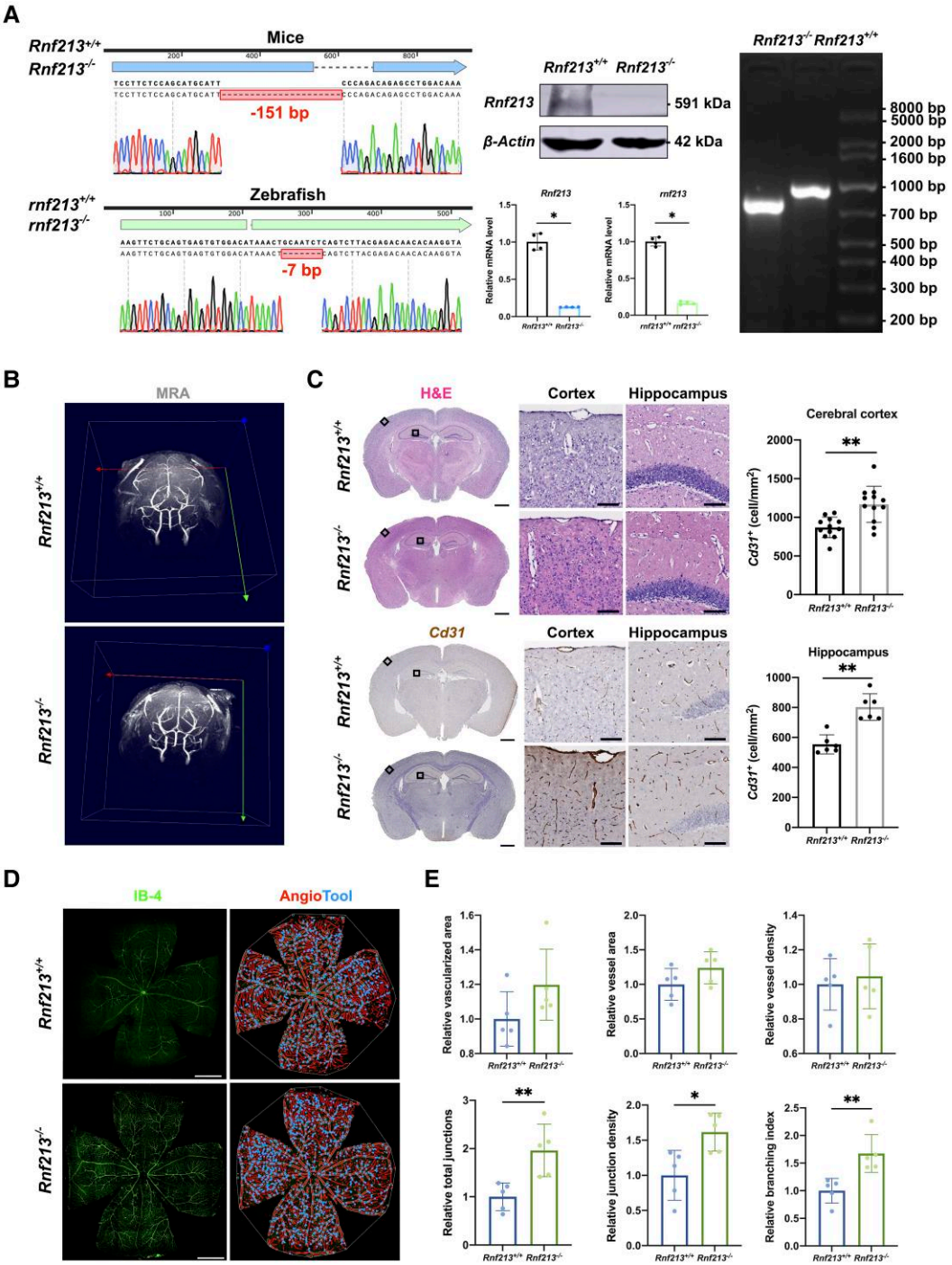

Figure 2 ***RNF213*** **deletion promotes pathological angiogenesis** ***in vivo***. (**A**) Sanger sequencing revealed a 151-bp deletion in mice and a 7-bp deletion in zebrafish. Western blots of mouse brain tissues validated an ~90% decrease in *Rnf213* expression in *Rnf213*$^{-/-}$ mice ($n = 4$, 1.00 ± 0.00 versus 0.07 ± 0.02, $P = 0.0286$). Quantitative RT-PCR confirmed the significantly reduced gene expression levels (*Rnf213*, $n = 4$, 1.00 ± 0.11 versus 0.13 ± 0.01, $P = 0.0286$; *rnf213*, $n = 4$, 0.99 ± 0.06 versus 0.17 ± 0.02, $P = 0.0286$). Agarose gel electrophoresis further confirmed this homozygous mutation in mice. (**B**) No significant differences in steno-occlusive arteries in the major branches of the Willis circle were observed between *Rnf213*$^{+/+}$ and *Rnf213*$^{-/-}$ mice using 7.0 T magnetic resonance angiography. (**C**) The complete structure of the cerebral vessels was stained with haematoxylin and eosin (H&E) and subjected to immunohistochemistry. From each section, one similar region of the hippocampus and three similar cortical regions in the unilateral cerebral hemisphere were randomly selected. The *Rnf213*$^{-/-}$ mice showed a significantly increased vessel density in both the cerebral cortex ($n = 12$, 868.77 ± 133.61 versus 1167.60 ± 234.25 cell/mm^2, $P = 0.0011$) and hippocampus ($n = 6$, 554.19 ± 63.98 versus 802.66 ± 88.41 cell/mm^2, $P = 0.0022$). Scale bar = 1 mm (*left*); scale bar = 100 μm (*right*). (**D**) Vessels throughout the retinas from *Rnf213*$^{+/+}$ and *Rnf213*$^{-/-}$ mice were labelled with IB-4. AngioTool software was used to automatically detect the vessel length (red) and junctions (blue). Scale bar = 500 μm. (**E**) No significant differences in the relative vascularized area ($n = 5$, 1.00 ± 0.16 versus 1.20 ± 0.21, $P = 0.0952$), vessel area ($n = 5$, 1.00 ± 0.23 versus 1.24 ± 0.23, $P = 0.2222$), and vessel density ($n = 5$, 1.00 ± 0.15 versus 1.05 ± 0.19, $P > 0.9999$) were observed between *Rnf213*$^{+/+}$ and *Rnf213*$^{-/-}$ mice. Compared to *Rnf213*$^{+/+}$ mice, *Rnf213*$^{-/-}$ mice showed significantly increased total junction numbers ($n = 5$, 1.00 ± 0.29 versus 1.96 ± 0.54, $P = 0.0079$), junction density ($n = 5$, 1.00 ± 0.35 versus 1.62 ± 0.27, $P = 0.0159$), and branch numbers ($n = 5$, 1.00 ± 0.25 versus 1.67 ± 0.34, $P = 0.0079$). Each dot represents one sample. The means ± SDs are shown. The dashed line indicates the region of interest. $^*P < 0.05$, $^{**}P < 0.01$, $^{***}P < 0.001$ and $^{****}P < 0.0001$.

Previous studies did not detect stenosis or occlusion of the intracranial arteries in *Rnf213*$^{+/+}$ mice or *Rnf213*$^{-/-}$ mice at the age of 16 to 64 weeks.[22,23] Although we extended the detection time to ~80 weeks, no significant differences in steno-occlusive changes in the major branches of the circle of Willis were observed in either mouse model using 7.0 T magnetic resonance angiography (MRA) (Fig. 2B and Supplementary Videos 1 and 2). Furthermore, we assessed whether *Rnf213*$^{-/-}$ mice exhibited other changes in pathological angiogenesis of the cerebral small vessels. The Human Protein Atlas (HPA) database showed that RNF213 protein concentrations were higher in the cerebral cortex and hippocampus than in other human tissues (Supplementary Fig. 2A). In addition, we found that *Rnf213* was expressed mainly in the cerebral small vessels but not the neurons in these areas using immunofluorescence (IF) staining, as shown in Supplementary Fig. 2B. Haematoxylin and eosin and IHC staining were then performed to visualize the complete structure of the brain and vessels in the *Rnf213*$^{+/+}$ mice and the *Rnf213*$^{-/-}$ mice. Using QuPath software to automatically calculate the regional density of *Cd31*$^{+}$ cells, we observed a significantly increased vessel density in the cerebral cortices and hippocampi of the *Rnf213*$^{-/-}$ mice compared with the *Rnf213*$^{+/+}$ *mice* (Fig. 2C). The relative increases in small arteries were then confirmed by performing IF staining (Supplementary Fig. 2C and D). In addition, we applied isolectin B4 (IB-4) to mark the whole retinal vessels and used AngioTool software[24] to automatically analyse and compare the vascular features of the *Rnf213*$^{+/+}$ mice and *Rnf213*$^{-/-}$ mice (Fig. 2D). The mature vascularized area of *Rnf213*$^{-/-}$ retinas was similar to that of *Rnf213*$^{+/+}$ retinas (Fig. 2E). Although no significant difference in vessel area or density was found between *Rnf213*$^{+/+}$ mice and *Rnf213*$^{-/-}$ mice, *Rnf213*$^{-/-}$ mice showed significantly greater total junction numbers, junction density and branching than *Rnf213*$^{+/+}$ mice (Fig. 2E). Moreover, coronal sections of the retina exhibited more vascular lumens near the macula in the *Rnf213*$^{-/-}$ mouse retinas (Supplementary Fig. 2E). These findings indicated the occurrence of pathological angiogenesis in the cerebral cortex, hippocampus and retinas in *Rnf213*$^{-/-}$ mice.

Thus, loss-of-function of *RNF213* may not be associated with the stenosis or occlusion of large cerebral arteries but may be positively correlated with angiogenesis of small arteries and/or arterioles.

Human brain microvascular endothelial cells are the major source of *RNF213*

RNF213 mutations were positively associated with pathological angiogenesis,[9,22,25–27] and the outgrowths of small vessels consisted primarily of irregular perforating small arteries and arterioles. Thus, we sought to identify the major source of *RNF213* among endothelial cells and other mural cells. Using donor STA serial sections from patients with intracranial aneurysm, we briefly compared the distribution of the RNF213 protein with that of other cell markers. The IHC analysis revealed that the RNF213 protein was expressed in the walls of all vessels but that RNF213 protein expression was higher in the tunica intima and media, as shown by the similar localization of the protein with endothelial and smooth muscle markers (Fig. 3A). Then, IF staining suggested that the RNF213 protein signal was significantly stronger in the tunica intima than in the tunica media, with a location similar to that of the endothelial marker *CD31* (Fig. 3B).

Using single-cell RNA sequencing (scRNA-seq) data from 25 human tissues and blood cells in the HPA, we found that *RNF213* mRNA expression in endothelial cells was higher than that in muscle and mesenchymal cells (Supplementary Fig. 3A). Although no endothelial or mural cell clusters were detected in the brain tissues using scRNA-seq, IHC revealed stronger RNF213 protein expression in endothelial cells than in glial or neuronal cells in the normal cortical sections (Supplementary Fig. 3B and C). Additionally, specific analyses of single cell types showed high expression of *RNF213* mRNA in the endothelial cell cluster from heart and eye tissues (Supplementary Fig. 3D and E), indicating that *RNF213* is expressed at higher levels in endothelial cells than in other vascular cells.

Furthermore, we compared *RNF213* protein and mRNA expression levels in different cellular components of primary cultured cerebral vascular cells. Although the RNF213 protein was commonly expressed in all cells, an increased fluorescence intensity was observed in human brain microvascular endothelial cells (HBMECs) (Fig. 3C). Additionally, immunoblot and qRT-PCR analyses confirmed that *RNF213* expression levels were higher in HBMECs than in other mural cells (Fig. 3D), indicating that HBMECs are the major sources of RNF213.

In addition, we explored the intracellular location of *RNF213* in HBMECs. The HPA database revealed that the RNF213 protein was a cytosol-localized protein in A431 cells (Supplementary Fig. 3F). Although the RNF213 protein was detected in both the cytoplasm and nucleus, fluorescence *in situ* hybridization (FISH) with an mRNA probe and IF staining confirmed that RNF213 was expressed mainly in the cytoplasm of HBMECs (Fig. 3E and F). In addition, neither signal peptide cleavage sites nor transmembrane helices were predicted to exist in the RNF213 protein using SignalP-5.0 and TMHMM-2.0 software, suggesting that it is not a classical secreted protein (Supplementary Fig. 3G and H). SecretomeP-2.0 software was used to predict secreted proteins lacking a conventional signal peptide that travel through the non-classical pathway and confirmed that the RNF213 protein is not a non-classical secreted protein (Supplementary Table 7). Thus, our findings indicated that RNF213 is a functional non-secreted cytosolic protein that is expressed primarily in cerebral endothelial cells.

Endothelial *RNF213* knockdown promotes cell proliferation, migration and angiogenesis

RNF213 is an anti-angiogenic protein that is expressed mainly in HBMECs; thus, the potential regulatory effects of loss-of-function of *RNF213* on cell proliferation, migration and tube formation were explored in this study. Small interfering RNA (siRNA) and short hairpin RNA (shRNA) sequences were designed to mimic *RNF213* loss-of-function conditions in a portion of MMD patients. The efficiency of specific *siRNF213* sequences was validated by western blotting and qRT-PCR (Fig. 4A).

The proliferation of HBMECs was measured by using a CCK-8 assay, a BrdU incorporation assay, and flow cytometry using EdU and Hoechst 33342 staining. Using the CCK-8 assay, we observed greater viability of *siRNF213*-treated HBMECs than *siNC*-treated HBMECs at 48 h and a significant increase in cell viability at 72 h (Fig. 4B). Cell proliferation was measured by competitive binding with BrdU/EdU or thymine during DNA replication. We randomly selected five locations to calculate the average numbers of DAPI^{+} cells and DAPI^{+}/BrdU^{+} cells. The ratio of DAPI^{+}/BrdU^{+} cells was significantly higher in *siRNF213*-treated HBMECs than in *siNC*-treated HBMECs (Fig. 4C). EdU and Hoechst 33342 were used to label proliferating cells and live cells, respectively. Flow cytometry analysis was applied to identify the ratio of EdU^{+}/Hoechst 33342^{+} cells in each

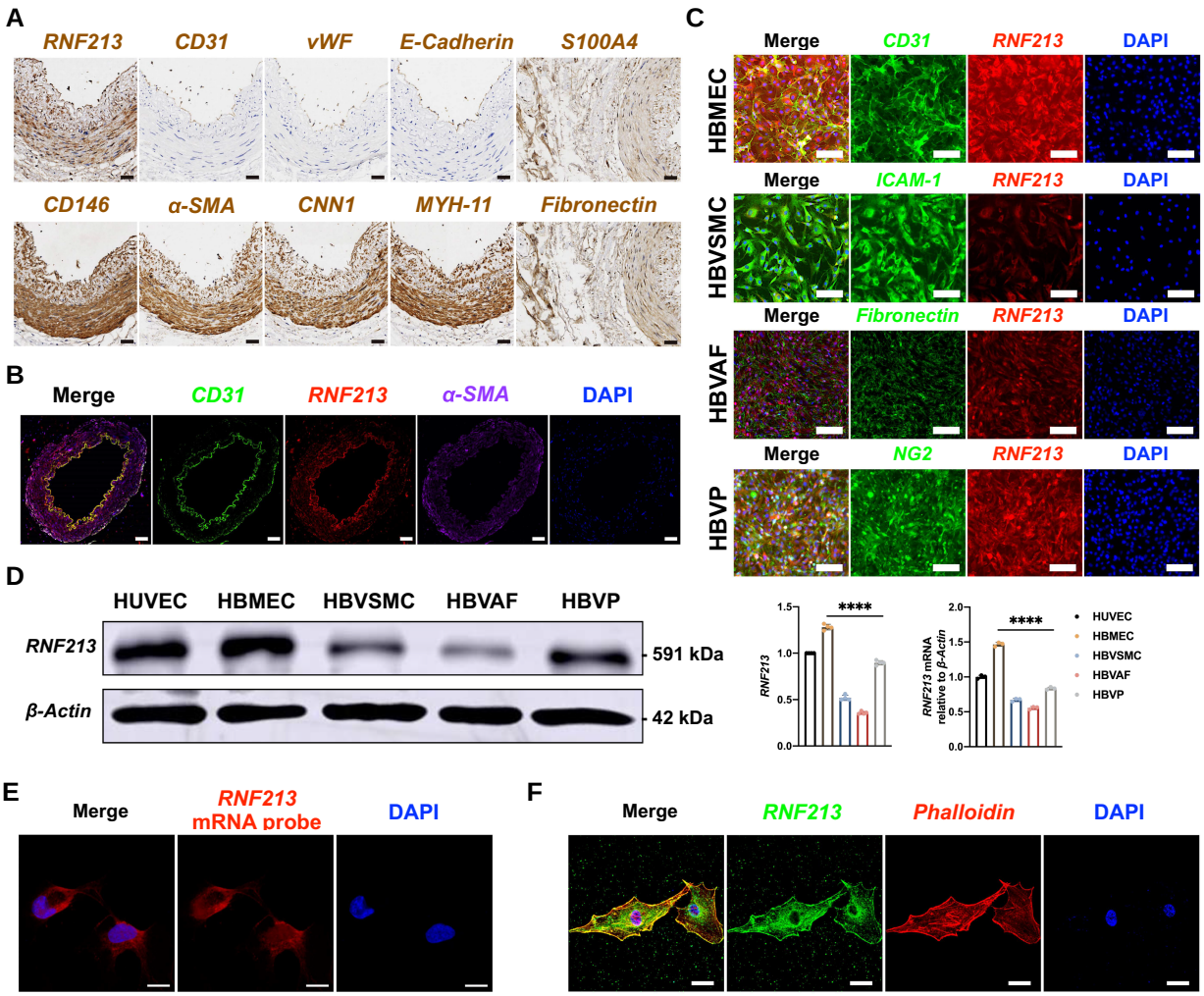

Figure 3 Human brain microvascular endothelial cells (HBMECs) are the major sources of *RNF213*. (**A**) Immunohistochemistry staining of donor superficial temporal artery sections from patients with intracranial aneurysm (IA). The RNF213 protein was expressed in all of the vascular walls. Endothelial markers [CD31, von Willebrand factor (vWF) and E-cadherin] were obviously located inside the vascular wall. Smooth muscle markers [α-SMA, calponin-1 (CNN1), smooth muscle myosin heavy chain 11 (MYH-11)] and pericyte markers (CD146 and α-SMA) were expressed mainly in the tunica media. Fibroblast markers (fibronectin and S100A4) were expressed mainly in the tunica adventitia. Scale bar = 20 μm. (**B**) The RNF213 protein co-localized with CD31 in the vascular wall. Scale bar = 50 μm. (**C**) The RNF213 protein was expressed at higher levels in human brain microvascular endothelial cells (HBMECs) and human brain vascular pericytes (HBVPs) than in human brain vascular adventitial fibroblasts (HBVAFs) or human brain vascular smooth muscle cells (HBVSMCs). Scale bar = 100 μm. (**D**) Using human umbilical vein endothelial cells (HUVECs) as controls, western blots revealed significantly higher RNF213 protein expression levels in HBMECs than in other cells ($n = 4$, 1.28 ± 0.03 versus 0.52 ± 0.03 versus 0.36 ± 0.01 versus 0.89 ± 0.02, $P < 0.0001$, Kruskal–Wallis statistic =14.12), which was confirmed by performing a qRT-PCR analysis ($n = 3$, 1.47 ± 0.03 versus 0.67 ± 0.02 versus 0.56 ± 0.02 versus 0.84 ± 0.02, $P < 0.0001$, Kruskal–Wallis statistic =10.38). (**E**) *RNF213* is mainly expressed in the cytoplasm of HBMECs, as shown by fluorescent *in situ* hybridization. Scale bar = 10 μm. (**F**) Confocal microscopy revealed stronger RNF213 protein expression in the cytoplasm than in the nucleus. Scale bar = 20 μm. Each dot represents one sample. The means ± SDs are shown. The dashed line indicates the region of interest. $^{*}P < 0.05$, $^{**}P < 0.01$, $^{***}P < 0.001$ and $^{****}P < 0.0001$.

group, and increased HBMEC proliferation was observed in the *siRNF213*-treated group (Fig. 4D).

Cell migration was evaluated using Transwell and wound healing assays. A membrane with a pore size of 8 μm was used to measure vertical HBMEC migration upon treatment with *siNC* and *siRNF213*. The number of HBMECs that migrated to the lower surface of the membrane was significantly greater in the *siRNF213*-treated group than in the *siNC*-treated group (Fig. 4E). Then, we constructed stable *RNF213*-knockdown HBMECs and inserted the *GFP* gene using lentiviral transfection. A two-well silicone insert was used to form a defined cell-free gap of 500 μm at 0 h, and HBMECs were continuously cultured in serum-free medium for another 48 h. The results showed a significantly decreased gap area and reduced gap depth at 24 h compared to those in control HBMECs, and the difference was more pronounced at 48 h (Fig. 4F), suggesting that horizontal HBMEC migration was increased.

We also explored the effect of *RNF213* loss on angiogenesis using tube formation assays, and we detected increases in the vascular area, density, length, number of vascular junctions and number of branches in *siRNF213*-treated HBMECs compared with *siNC*-treated HBMECs, as shown in Fig. 4G and H. In summary, our findings suggest that *RNF213* knockdown promotes HBMEC proliferation, migration and angiogenesis *in vitro* and thus that *RNF213* plays an important role in MMD pathogenesis.

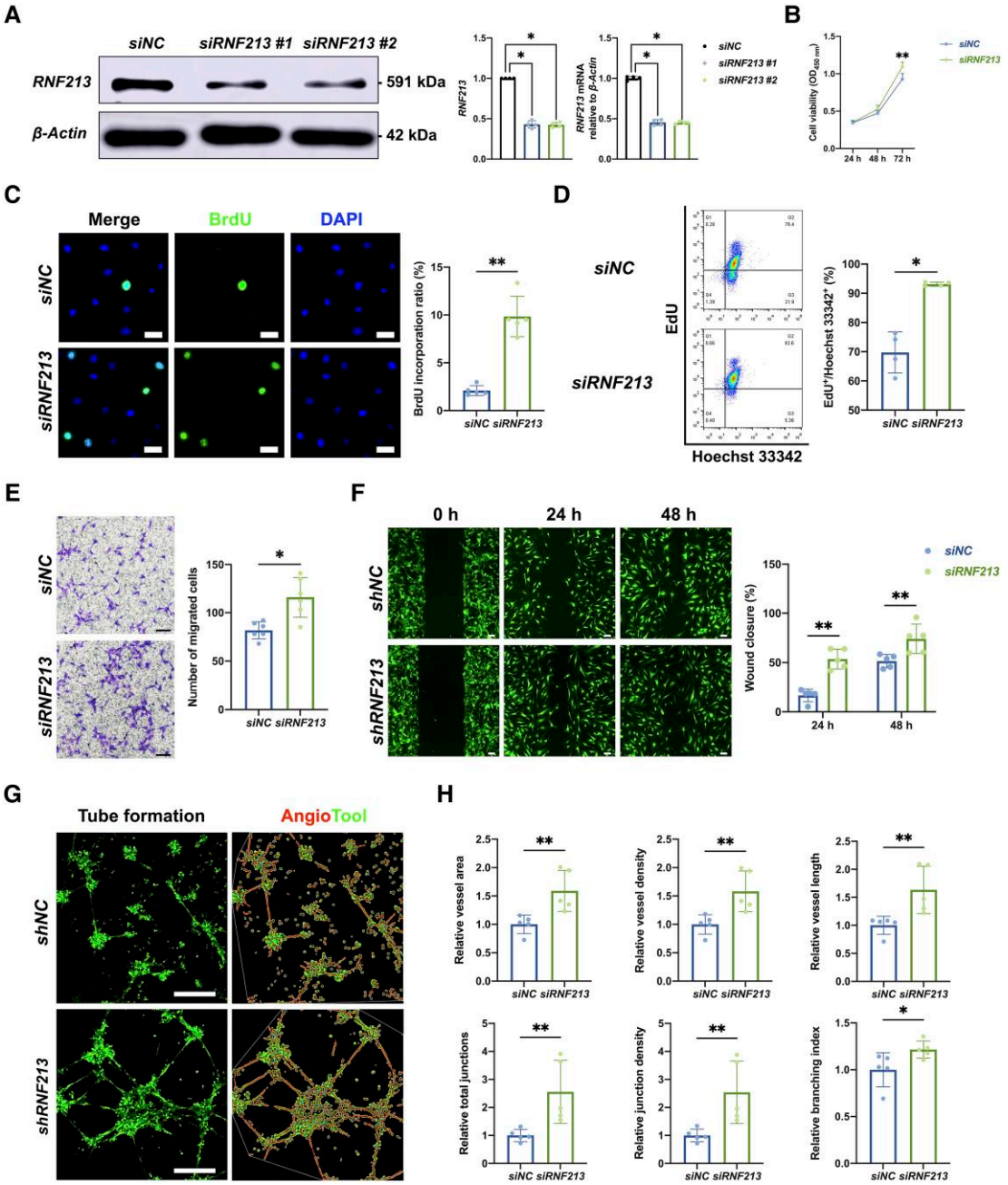

Figure 4 Endothelial *RNF213* knockdown promotes HBMEC proliferation, migration and angiogenesis. (**A**) Two designed siRNA/shRNA sequences were used to mimic *RNF213* loss-of-function conditions, which were confirmed by western blot (*siNC* versus *siRNF213* #1: $n = 4$, 1.00 ± 0.00 versus 0.43 ± 0.05, $P = 0.0286$; *siNC* versus *siRNF213* #2: $n = 4$, 1.00 ± 0.00 versus 0.42 ± 0.03, $P = 0.0286$) and qRT-PCR analyses (*siNC* versus *siRNF213* #1: $n = 4$, 1.00 ± 0.03 versus 0.45 ± 0.04, $P = 0.0286$; *siNC* versus *siRNF213* #2: $n = 4$, 1.00 ± 0.03 versus 0.45 ± 0.02, $P = 0.0286$). (**B**) The *siRNF213*-treated human brain microvascular endothelial cells (HBMECs) showed greater cell viability than the *siNC*-treated HBMECs at 48 h ($n = 6$, 0.47 ± 0.03 versus 0.52 ± 0.05, $P = 0.0931$) and also showed significantly greater cell viability at 72 h ($n = 6$, 0.93 ± 0.07 versus 1.09 ± 0.06, $P = 0.004$) based on the results of CCK-8 assays. (**C**) A BrdU incorporation assay was conducted to measure the proliferation of *siNC*- and *siRNF213*-treated HBMECs. The *siRNF213*-treated HBMECs showed a significantly greater BrdU incorporation ratio than the *siNC*-treated HBMECs ($n = 5$, 2.09 ± 0.47 versus $9.84 \pm 1.89\%$, $P = 0.0079$). Scale bar = 20 μm. (**D**) Flow cytometry was used to assess the proliferation of *siNC*- and *siRNF213*-treated HBMECs after labelling with EdU and Hoechst 33342. The *siRNF213*-treated HBMECs showed a significantly greater cell proliferation ratio than the *siNC*-treated HBMECs ($n = 4$, 69.75 ± 6.07 versus $93.15 \pm 0.62\%$, $P = 0.0286$). (**E**) Transwell assays were performed to measure vertical HBMEC migration. *siRNF213*-treated HBMECs showed greater vertical migration than *siNC*-treated HBMECs ($n = 6$, 86.25 ± 38.92 versus 124.75 ± 57.69, $P = 0.0152$). Scale bar = 100 μm. (**F**) A wound healing assay was used to measure horizontal HBMEC migration. The *siRNF213*-treated HBMECs showed markedly greater horizontal migration than the *siNC*-treated HBMECs at 24 h ($n = 5$, 16.16 ± 6.44 versus 55.45 ± 9.20, $P = 0.0079$) and 48 h ($n = 5$, 49.76 ± 5.26 versus 73.36 ± 14.78, $P = 0.0079$). Scale bar = 100 μm. (**G**) A tube formation assay was performed to measure HBMEC angiogenesis. AngioTool software was used to automatically detect the vessel length (red) and junctions (green). Scale bar = 100 μm. (**H**) The *siRNF213*-treated HBMECs showed significantly greater vessel area ($n = 5$, 1.00 ± 0.16 versus 1.59 ± 0.36, $P = 0.0079$), vessel density ($n = 5$, 1.00 ± 0.17 versus 1.58 ± 0.36, $P = 0.0079$), vessel length ($n = 5$, 1.00 ± 0.16 versus 1.63 ± 0.42, $P = 0.0079$), total number of junctions ($n = 5$, 1.00 ± 0.22 versus 2.56 ± 1.13, $P = 0.0079$), junction density ($n = 5$, 1.00 ± 0.23 versus 2.54 ± 1.12, $P = 0.0079$), and branching index values ($n = 5$, 1.00 ± 0.18 versus 1.22 ± 0.09, $P = 0.0317$) than the *siNC*-treated HBMECs. Each dot represents one sample. The means ± SDs are shown. The dashed line indicates the region of interest. $^{*}P < 0.05$, $^{**}P < 0.01$, $^{***}P < 0.001$ and $^{****}P < 0.0001$.

The Hippo pathway is associated with *RNF213*-related MMD pathogenesis

In this study, RNA-seq was performed to determine the potential mechanism of *RNF213* mutations in MMD by using HBMECs and donor STA samples. Data were analysed and processed using the protocol outlined in Supplementary Fig. 4A. After gene annotation and quality control (Supplementary Fig. 4B and Supplementary Table 8), genes with a count < 2% and/or a degree of variation < 5% were filtered, and a differential expression analysis was performed with the *edgeR* package.

First, a total of 2633 differentially expressed genes (DEGs) between *siNC*-treated and *siRNF213*-treated HBMECs were identified using the Network Analyst platform (v3.0),[28] as shown in Fig. 5A. The top 100 significantly upregulated and downregulated DEGs were selected based on adjusted *P*-values (Supplementary Fig. 4C and Supplementary Table 9). The Database for Annotation, Visualization and Integrated Discovery (DAVID) bioinformatics resource (v6.8)[29] was then used to discover the biological functions in which each of the genes was enriched. We obtained 136 significantly enriched Gene Ontology (GO)[30] terms from the top 100 upregulated DEGs, among which the biological processes were positively associated with the development of the vasculature (Fig. 5B and Supplementary Table 10). We identified 45 significantly enriched GO terms for the top 100 downregulated DEGs, among which the biological processes were negatively related to cell adhesion and endothelial cell proliferation (Fig. 5B and Supplementary Table 10). Then, 78 important signalling pathways from the Kyoto Encyclopedia of Genes and Genomes (KEGG) database were screened for all DEGs[31]; these pathways were associated primarily with transcription and translation, biological metabolism, the cell cycle and proliferation (Fig. 5C and Supplementary Tables 11 and 12). In addition, we identified 584 DEGs between STAs from intracranial aneurysm patients and STAs from MMD patients carrying the *RNF213* mutation (p.R4810K) using the same approach (Fig. 5D), and the top 100 upregulated and downregulated DEGs were used for functional annotations (Supplementary Fig. 4C and Supplementary Table 13). Bioinformatics analyses revealed 185 positively enriched GO terms, 60 negatively enriched GO terms and 56 KEGG pathways associated with MMD pathogenesis, as shown in Fig. 5E and F (Supplementary Tables 14–16). Among these pathways, 29 signalling pathways enriched in the *siRNF213*-treated HBMECs and MMD arteries were screened (Supplementary Fig. 4D), mainly cell proliferation and junction-associated pathways.

According to previous research, the Hippo signalling pathway might play key roles in vascular remodelling and barrier formation.[32] The Hippo signalling pathway was suppressed in our study via reduced gene expression, and its suppression was positively associated with the proliferation of vascular disease. We similarly observed impaired adherens junctions and tight junctions in MMD patients with the *RNF213* p.R4810K mutation (Supplementary Fig. 4E); this impairment might inhibit Hippo signalling. Although researchers have not clearly determined whether Hippo signalling is the major pathway involved in MMD pathogenesis, our findings indicate that the pathogenic *RNF213* mutation may participate in regulating the Hippo signalling pathway.

Endothelial *RNF213* knockdown activates the Hippo effector YAP/TAZ

We measured the levels of key molecules in *RNF213*-knockdown HBMECs to explore the effect of *RNF213* mutations on the Hippo pathway. The transcriptional co-activators Yes-associated protein 1 (*YAP*) and tafazzin (*TAZ*) are master regulators of the Hippo signalling pathway.[33] In brief, *MST1/2* phosphorylate and activate *LATS1/2*, which then phosphorylate *YAP/TAZ*, leading to the cytoplasmic sequestration, degradation and inactivation of *YAP/TAZ*. However, *YAP/TAZ* shuttle from the cytosol to the nucleus, where they mainly interact with *TEAD* transcription factors to regulate the expression of a large group of target genes primarily involved in cell growth, survival and migration.

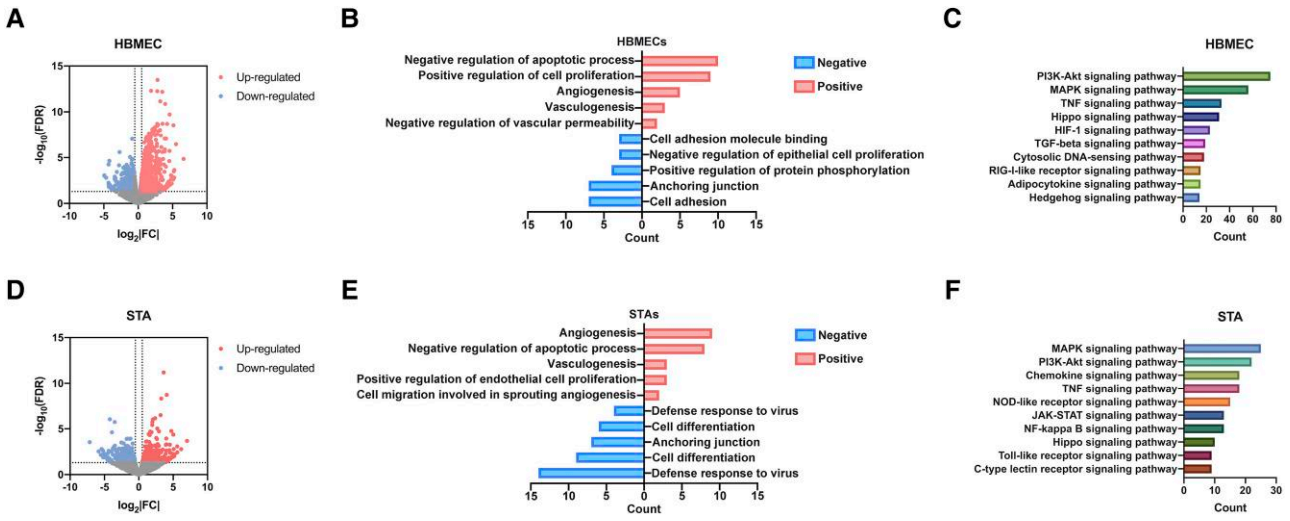

Figure 5 The Hippo signalling pathway might be involved in *RNF213*-related MMD pathogenesis, as shown through bioinformatics analyses. (**A**) Volcano plot showing 2633 differentially expressed genes (DEGs) between *siNC*- and *siRNF213*-treated human brain microvascular endothelial cell (HBMECs), including 1431 upregulated (red) and 1202 downregulated (blue) DEGs. (**B**) GO analysis indicated functions that were positively and negatively regulated by the top 100 *RNF213*-related DEGs. (**C**) Functional enrichment analysis of pathways significantly enriched in the *RNF213*-related DEGs. (**D**) Volcano plot showing 584 DEGs between intracranial aneurysm (IA) donor superficial temporal arteries and moyamoya disease (MMD) donor superficial temporal arteries, including 301 upregulated (red) and 283 downregulated (blue) DEGs. (**E**) GO analysis of functions that were positively and negatively regulated by the top 100 MMD-related DEGs. (**F**) Functional enrichment analysis of pathways significantly enriched in MMD-related DEGs.

The key upstream molecules of *MST1/2* and *LATS1/2* were explored in *siRNF213*-treated HBMECs compared with *siNC*-treated HBMECs using western blot analyses (Supplementary Fig. 5A). Quantitative RT-PCR analyses revealed increased *TAZ* and *YAP* mRNA expression levels between the groups (Supplementary Fig. 5B). The RNA polymerase inhibitor actinomycin D (ActD) was then applied to determine whether this finding was due to transcriptional activation or increased mRNA stability. After incubation with ActD (500 μg/ml) for 30 min, qRT-PCR analyses confirmed elevated transcription of *TAZ* and *YAP* in *siRNF213*-treated HBMECs (Supplementary Fig. 5B). In addition, *TAZ* mRNA expression levels were significantly higher in *siRNF213*-treated HBMECs incubated with ActD for an extended period of 0–6 h than in control HBMECs (Supplementary Fig. 5C).

Furthermore, we measured the levels of active (unphosphorylated) and inactive (phosphorylated) YAP/TAZ proteins. Significantly reduced p-TAZ/TAZ ratios and p-YAP/YAP ratios were detected at the total protein level in *siRNF213*-treated HBMECs (Fig. 6A). The intracellular distribution of active YAP/TAZ was then explored in this study. Although cytoplasmic YAP/TAZ protein levels were slightly reduced, the nuclear YAP/TAZ level was significantly increased (Fig. 6B and C), and its nuclear translocation ratio was elevated in *siRNF213*-treated HBMECs (Fig. 6D and E). Moreover, a stronger YAP/TAZ fluorescence intensity was detected in donor STA sections from MMD patients with *RNF213* mutations than in those from patients with intracranial aneurysm (Supplementary Fig. 5D). Co-immunoprecipitation (Co-IP) experiments confirmed a direct protein–protein interaction between RNF213 and YAP/TAZ (Supplementary Fig. 5A). Thus, *RNF213* knockdown promotes *YAP/TAZ* activation.

Endothelial *RNF213* knockdown promotes *VEGFR2* expression via *YAP/TAZ-TEAD*

We measured the intranuclear levels of transcription factors in the Hippo pathway, and qRT-PCR analyses revealed prominently elevated *TEAD1-3* mRNA expression levels and reduced *TEAD4* mRNA expression levels in *siRNF213*-treated HBMECs (Supplementary Fig. 5E), which indicated that Hippo signalling was switched to an 'off' state through the upregulation of *YAP/TAZ* and *TEADs*. Interactive *YAP/TAZ-TEAD* binding activates classic regulators of cell growth and organogenesis, including *Axin2*, *cycD*, *Sox2*, *Nkd1*, *myc*, *Slug*, *Birc2/5*, *CTGF* and *Gh2*.[33] Among these well studied molecules, *VEGFR2*, an important gene regulating vascular development via the *VEGF-VEGFR2* axis, was recently identified as a downstream target molecule of *YAP/TAZ-TEAD*.[34] Therefore, we tested whether *RNF213* knockdown activated *VEGFR2* expression to promote pathological angiogenesis through interactive *YAP/TAZ-TEAD* binding.

Although the ratio of *VEGFR2* phosphorylated at different sites (p-VEGFR2) to VEGFR2 varied in *siRNF213*-treated HBMECs (Fig. 7A), flow cytometry analysis showed a marked increase in VEGFR2 signals in *siRNF213*-treated HBMECs compared with *siNC*-treated HBMECs (Supplementary Fig. 5F). Significantly increased membrane protein expression and decreased intracellular protein expression of VEGFR2 were detected in *siRNF213*-treated HBMECs (Fig. 7B), and qRT-PCR confirmed the increase in *VEGFR2* mRNA expression (Supplementary Fig. 5B). In addition, post-translational modifications (PTMs) of the VEGFR2 protein depend on cytoplasmic organelles, and mature proteins are transferred from the Golgi apparatus to the cell surface. We detected the co-localization of VEGFR2 and the Golgi apparatus marker TGN46 and found that *RNF213* knockdown increased the distribution of VEGFR2 in the Golgi apparatus, which may suggest an increase in PTMs (Fig. 7C). Our data indicate that loss of endothelial *RNF213* promotes overexpression of VEGFR2 through 'off-state' Hippo signalling.

Inhibition of *YAP/TAZ* expression reverses *RNF213* knockdown-induced angiogenesis

YAP/TAZ expression was inhibited via RNAi or incubation with *YAP/TAZ* inhibitor-1 (50 nmol/ml) for 24 h to further explore the major role of *YAP/TAZ* in *RNF213* knockdown-induced angiogenesis. The decrease in YAP/TAZ protein expression was consistent with an obvious reduction in VEGFR2 protein expression, and the inhibition of *YAP/TAZ* expression in inhibitor-treated HBMECs alleviated *VEGFR2* overexpression at the protein level (Fig. 7D). This finding was subsequently confirmed by qRT-PCR (Supplementary Fig. 5G). A dual-luciferase reporter assay previously showed that *YAP/TAZ* induces the transcription of *VEGFR2*.[34] In addition, we found that inhibition of *YAP/TAZ* reduced the YAP/TAZ distribution in the nucleus and increased the VEGFR2 distribution in the Golgi apparatus (Supplementary Figs 5H and 7C).

VEGF is generally accepted as a proangiogenic factor that regulates vascular remodelling by binding cell-surface VEGFR2. Thus, a small dose of $VEGF_{165}$ (5 ng/ml) was applied for 0–6 h to explore the time-dependent effect of *VEGF* on *TAZ* expression in HBMECs. Quantitative RT-PCR analysis revealed that *TAZ* mRNA expression peaked at 2 h (Fig. 7E). Next, a tube formation assay was employed using *siRNF213*-treated HBMECs incubated with a *YAP/TAZ* inhibitor and/or $VEGF_{165}$ (Fig. 7F). Loss of endothelial *TAZ* restricted tube formation, while stimulation of *TAZ* expression enhanced vasculogenesis (Fig. 7G). These findings suggest that endothelial *YAP/TAZ* expression is positively associated with tube formation and that *YAP/TAZ* inhibition reverses *RNF213* knockdown-induced angiogenesis.

External validation of Hippo pathway dysregulation using *RNF213*-deficient animals

Vascular endothelial cells were isolated from *RNF213*-deficient animals and used to measure key molecules in the Hippo pathway for further verification. Since the vascular endothelial cells of the Tg(*flk:EGFR; gata1:DsRed*) transgenic line exhibited systemic green autofluorescence but those of normal zebrafish (*AB line*) did not, fluorescence-activated cell sorting (FACS) was used to separate the endothelial cells from single-cell suspensions derived from $rnf213^{+/+}$ and $rnf213^{-/-}$ zebrafish at 120 h post-fertilization (hpf) (Supplementary Fig. 6A). An insufficient number of antibodies is an acknowledged obstacle in zebrafish research; thus, we measured the mRNA expression levels of *taz*, *yap* and *vegfr2*. Endothelial cells from the $rnf213^{-/-}$ zebrafish exhibited significantly higher *taz*, *yap* and *vegfr2* levels than those from the $rnf213^{+/+}$ zebrafish (Supplementary Fig. 6B).

Furthermore, we extracted vascular endothelial cells from the brains of $Rnf213^{+/+}$ and $Rnf213^{-/-}$ mice at 64–80 weeks of age (Supplementary Fig. 6C). Endothelial deletion of *Rnf213* not only promoted *Taz*, *Yap* and *Vegfr2* mRNA expression (Supplementary Fig. 6B) but also significantly increased nuclear *Taz* and *Yap* expression and surface *Vegfr2* expression (Supplementary Fig. 6D). In addition, endothelial deletion of *Rnf213* increased the level of nuclear YAP/TAZ expression, and a marked increase in cell-surface *Vegfr2* expression was observed in endothelial cells from $Rnf213^{-/-}$ mice (Supplementary Fig. 6E). These findings support the hypothesis

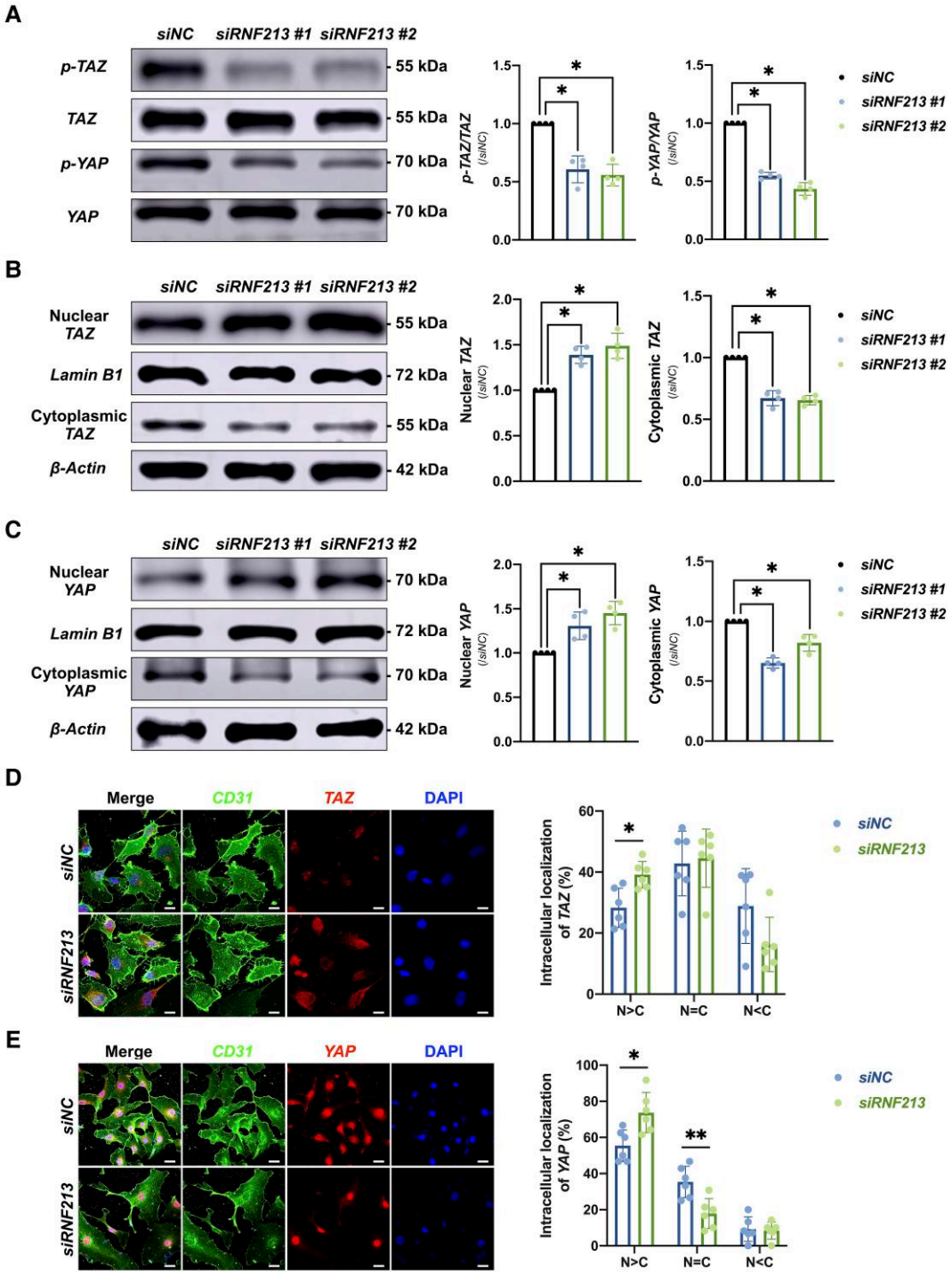

Figure 6 Endothelial *RNF213* knockdown activates the Hippo effectors *TAZ* and *YAP*. (**A**) Quantitative analysis of p-TAZ/TAZ and p-YAP/YAP protein levels in *siNC*- and *siRNF213*-treated HBMECs (p-TAZ/TAZ, $n = 4$, *siNC* versus *siRNF213 #1* = 1.00 ± 0.00 versus 0.61 ± 0.12, $P = 0.0286$; *siNC* versus *siRNF213 #2* = 1.00 ± 0.00 versus 0.56 ± 0.09, $P = 0.0286$; p-YAP/YAP, $n = 4$, *siNC* versus *siRNF213 #1* = 1.00 ± 0.00 versus 0.55 ± 0.03, $P = 0.0286$; *siNC* versus *siRNF213 #2* = 1.00 ± 0.00 versus 0.43 ± 0.05, $P = 0.0286$). (**B**) Quantitative analysis of nuclear (N) and cytoplasmic (C) TAZ protein levels in *siNC*- and *siRNF213*-treated HBMECs at the nuclear and cytoplasmic levels (nuclear TAZ, $n = 4$, *siNC* versus *siRNF213 #1* = 1.00 ± 0.00 versus 1.39 ± 0.09, $P = 0.0286$; *siNC* versus *siRNF213 #2* = 1.00 ± 0.00 versus 1.49 ± 0.14, $P = 0.0286$; cytoplasmic TAZ, $n = 4$, *siNC* versus *siRNF213 #1* = 1.00 ± 0.00 versus 0.67 ± 0.06, $P = 0.0286$; *siNC* versus *siRNF213 #2* = 1.00 ± 0.00 versus 0.66 ± 0.04, $P = 0.0286$). (**C**) Quantitative analysis of nuclear and cytoplasmic YAP protein levels in *siNC*- and *siRNF213*-treated HBMECs at the nuclear and cytoplasmic levels (nuclear YAP, $n = 4$, *siNC* versus *siRNF213 #1* = 1.00 ± 0.00 versus 1.31 ± 0.16, $P = 0.0286$; *siNC* versus *siRNF213 #2* = 1.00 ± 0.00 versus 1.45 ± 0.13, $P = 0.0286$; cytoplasmic YAP, $n = 4$, *siNC* versus *siRNF213 #1* = 1.00 ± 0.00 versus 0.65 ± 0.04, $P = 0.0286$; *siNC* versus *siRNF213 #2* = 1.00 ± 0.00 versus 0.82 ± 0.07, $P = 0.0286$). (**D**) Analysis of the difference in the distribution of TAZ protein expression between *siNC*- and *siRNF213*-treated HBMECs (N > C, $n = 6$, 28.30 ± 6.42 versus 39.16 ± 4.33%, $P = 0.0152$; N = C, $n = 6$, 42.83 ± 10.61 versus 44.55 ± 9.51%, $P > 0.9999$; N < C, $n = 6$, 28.87 ± 12.25 versus 16.29 ± 8.89%, $P = 0.0931$). Scale bar = 20 μm. (**E**) Analysis of the difference in the distribution of YAP protein expression between *siNC*- and *siRNF213*-treated HBMECs (N > C, $n = 6$, 55.42 ± 8.72 versus 73.75 ± 11.09%, $P = 0.0152$; N = C, $n = 6$, 35.34 ± 8.67 versus 17.87 ± 8.22%, $P = 0.0087$; N < C, $n = 6$, 9.25 ± 6.78 versus 8.39 ± 4.71%, $P = 0.7879$). Scale bar = 20 μm. Each dot represents one sample. The means ± SDs are shown. The dashed line indicates the region of interest. $^{*}P < 0.05$, $^{**}P < 0.01$, $^{***}P < 0.001$, $^{****}P < 0.0001$.

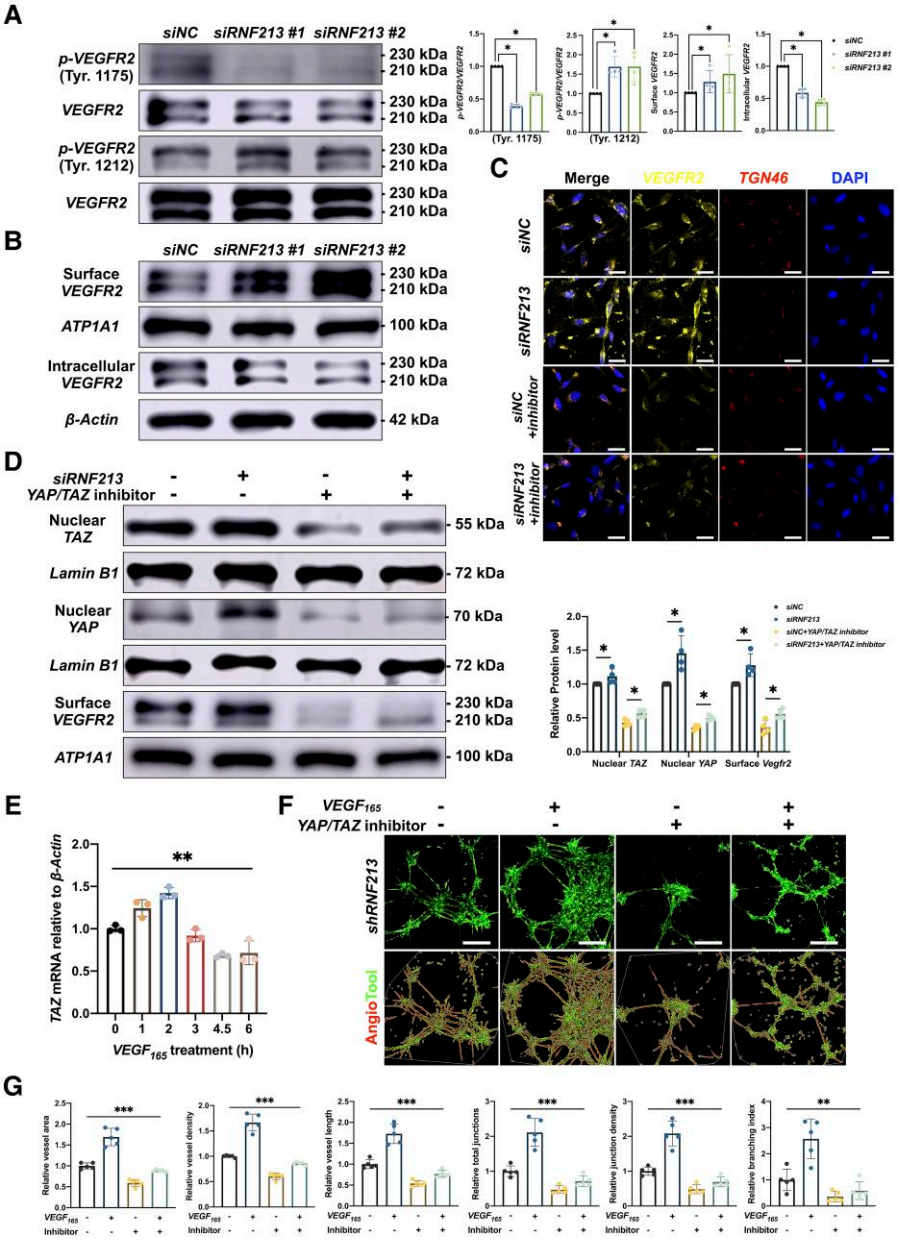

Figure 7 Inhibition of YAP/TAZ expression reverses *RNF213*-induced angiogenesis. (**A**) Quantitative analysis of the p-VEGFR2/VEGFR2 protein ratio in *siNC*- and *siRNF213*-treated HBMECs (Tyr.1175, $n = 4$, *siNC* versus *siRNF213 #1* = 1.00 ± 0.00 versus 0.39 ± 0.03, $P = 0.0286$; *siNC* versus *siRNF213 #2* = 1.00 ± 0.00 versus 0.57 ± 0.02, $P = 0.0286$; Tyr.1212, $n = 4$, *siNC* versus *siRNF213 #1* = 1.00 ± 0.00 versus 1.69 ± 0.26, $P = 0.0286$; *siNC* versus *siRNF213 #2* = 1.00 ± 0.00 versus 1.70 ± 0.37, $P = 0.0286$). (**B**) Quantitative analysis of surface and intracellular VEGFR2 protein levels between *siNC*- and *siRNF213*-treated HBMECs (surface VEGFR2, $n = 4$, *siNC* versus *siRNF213 #1* = 1.00 ± 0.00 versus 1.28 ± 0.29, $P = 0.0286$; *siNC* versus *siRNF213 #2* = 1.00 ± 0.00 versus 1.49 ± 0.50, $P = 0.0286$; intracellular VEGFR2, $n = 4$, *siNC* versus *siRNF213 #1* = 1.00 ± 0.00 versus 0.59 ± 0.06, $P = 0.0286$; *siNC* versus *siRNF213 #2* = 1.00 ± 0.00 versus 0.44 ± 0.04, $P = 0.0286$). (**C**) Analysis of the VEGFR2 protein distribution between *siNC*- and *siRNF213*-treated HBMECs. Scale bar = 20 μm. (**D**) Quantitative analysis of nuclear TAZ, nuclear YAP, and surface VEGFR2 protein levels in *siNC*-, *siRNF213*–, *siNC*+YAP/TAZ inhibitor-1–, and *siRNF213* +YAP/TAZ inhibitor-1-treated HBMECs (nuclear TAZ, $n = 4$, *siNC* versus *siRNF213* = 1.00 ± 0.00 versus 1.11 ± 0.11, $P = 0.0286$; *siNC*+YAP/TAZ inhibitor-1 versus *siRNF213*+YAP/TAZ inhibitor-1 = 0.43 ± 0.05 versus 0.56 ± 0.06, $P = 0.0286$; nuclear YAP, $n = 4$, *siNC* versus *siRNF213* = 1.00 ± 0.00 versus 1.46 ± 0.26, $P = 0.0286$; *siNC*+YAP/TAZ inhibitor-1 versus *siRNF213*+YAP/TAZ inhibitor-1 = 0.36 ± 0.03 versus 0.50 ± 0.04, $P = 0.0286$; surface *VEGFR2*, $n = 4$, *siNC* versus *siRNF213* = 1.00 ± 0.00 versus 1.28 ± 0.17, $P = 0.0286$; *siNC*+YAP/TAZ inhibitor-1 versus *siRNF213*+YAP/TAZ inhibitor-1 = 0.36 ± 0.10 versus 0.56 ± 0.07, $P = 0.0286$). (**E**) Quantitative analysis of *TAZ* mRNA levels in normal HBMECs incubated with $VEGF_{165}$ (5 ng/ml) at 0, 1, 2, 3, 4.5 and 6 h ($n = 3$, 1.00 ± 0.04 versus 1.24 ± 0.10 versus 1.42 ± 0.07 versus 0.92 ± 0.07 versus 0.68 ± 0.02 versus 0.72 ± 0.14, $P = 0.0086$, Kruskal–Wallis statistic =15.46). (**F**) A tube formation assay was conducted to measure angiogenesis in *siRNF213*-treated HBMECs after incubation with a YAP/TAZ inhibitor and/or $VEGF_{165}$. Scale bar = 100 μm. (**G**) AngioTool software was used to automatically detect the vessel length and junctions. The *siRNF213*-transfected HBMECs treated with a YAP/TAZ inhibitor showed significant reductions in the vessel area ($n = 6$, 1.00 ± 0.07 versus 1.69 ± 0.21 versus 0.59 ± 0.08 versus 0.89 ± 0.03, $P = 0.0005$, Kruskal–Wallis statistic =17.58), vessel density ($n = 6$, 1.00 ± 0.02 versus 1.66 ± 0.17 versus 0.60 ± 0.07 versus 0.86 ± 0.03, $P = 0.0005$, Kruskal–Wallis statistic =17.86), vessel length ($n = 6$, 1.00 ± 0.41 versus 2.57 ± 0.76 versus 0.36 ± 0.20 versus 0.59 ± 0.34, $P = 0.0044$, Kruskal–Wallis statistic =13.09), total number of junctions ($n = 6$, 1.00 ± 0.15 versus 2.11 ± 0.40 versus 0.47 ± 0.11 versus 0.71 ± 0.15, $P = 0.0007$, Kruskal–Wallis statistic =16.91), junction density ($n = 6$, 1.00 ± 0.12 versus 2.08 ± 0.36 versus 0.48 ± 0.13 versus 0.69 ± 0.14, $P = 0.0009$, Kruskal–Wallis statistic =16.51), and branching index ($n = 6$, 1.00 ± 0.10 versus 1.73 ± 0.24 versus 0.54 ± 0.07 versus 0.77 ± 0.08, $P = 0.0005$, Kruskal–Wallis statistic =17.86) compared to those of *siRNF213*-transfected HBMECs treated with $VEGF_{165}$. Each dot represents one sample. The means ± SDs are shown. The dashed line indicates the region of interest. $^{*}P < 0.05$, $^{**}P < 0.01$, $^{***}P < 0.001$, $^{****}P < 0.0001$.

that loss-of-function of *RNF213* increases *VEGFR2* expression by activating the Hippo effector *YAP/TAZ*.

Discussion

Although missense SNPs in the *RNF213* gene have been studied for more than 10 years using peripheral blood or saliva samples from MMD patients, our data indicated that STA samples from some patients with sporadic MMD contained a novel CNV deletion that markedly damaged RNF213 protein structure and function, as shown through WGS analysis. Homozygosity of MMD-specific pathogenic mutations was present in the arteries, and heterozygosity was present in the blood samples. These differences suggest that environmental factors might exacerbate *RNF213* mutation in MMD vascular lesions. However, MMD lesions should be located primarily in steno-occlusive areas and moyamoya vessels. Due to ethical and legal restrictions, we could not obtain these samples during surgical revascularization. Donor STAs were the best alternative tissue samples, but the results from such samples may not completely reflect the precise pathogenesis of MMD. Nevertheless, loss-of-function *RNF213* mutations in MMD were detectable.

Our findings from donor artery sections confirmed that thickening of the tunica intima and thinning of the tunica media are two main pathological characteristics of MMD in patients. However, the pathogenic *RNF213* p.R4810K mutation was positively associated with concentric intimal hyperplasia only, and changes in the number of smooth muscle fibres were not explained by these mutations. Although quantitative analyses indicated that HBMECs were the major source of *RNF213*, higher expression was detected in smooth muscle cells (SMCs) within arterial and heart tissues than in fibroblasts. The limited research on the effect of *RNF213* mutation on smooth muscle remains controversial. *In vitro* studies using induced pluripotent stem cell-derived SMCs have demonstrated that *RNF213* mutation does not damage the cellular proliferation, migration, and contraction abilities of SMCs in MMD patients.[35] A co-culture study has confirmed that smooth muscle progenitor cells are recruited and regulated by endothelial colony-forming cells in MMD patients.[36] In contrast, morpholino-based *rnf213* knockdown of zebrafish results in marked decreases in myofibrils and motor neurons.[37] Since mutations in the smooth muscle marker *ACTA2* have been reported in some family numbers of MMD patients and as phenotypic conversion of SMCs is regulated by circZXDC, which is involved in MMD pathogenesis,[38,39] we did not explore the effect of *RNF213* on smooth muscles. Because MMD is a chronic and progressive disease, a minimum change in SMCs from *RNF213* mutation could be obtained in a long-term observation.

In addition, *RNF213* is expressed at high levels in immune cells (the highest levels were detected in peripheral NK and T cells) and plays a key role in resisting bacterial infection via the ubiquitylation of lipopolysaccharide.[40] Recent studies have revealed that dysregulated *RNF213* function is associated with autoimmune diseases.[41,42] Nevertheless, our study did not explore the potential immunomodulation of *RNF213* in angiogenesis. Such research might provide new insights into MMD pathogenesis in future studies.

Some of the most important features of MMD are steno-occlusive changes in the distal portions of the internal carotid arteries and/or the proximal portion of the circle of Willis.[1] Similar to the case in previous studies,[22,23] MRA did not reveal significant differences in the major arteries of the head and neck in *Rnf213*$^{-/-}$ mice. However, another feature of MMD is abnormally proliferative vasculopathy consisting of artery and arteriole proliferation.[1] We observed increased vessel size, number and density in the cerebral cortex, hippocampus and retinas of *Rnf213*$^{-/-}$ mice. Using *rnf213*$^{-/-}$ zebrafish, we have previously observed similar blood vessel sprouting in the intersegmental arteries at 72 hpf and detected a possible mulberry-like cluster of disordered-flow vascular channels at 120 hpf.[25,26] Our study showed that loss-of-function of *RNF213* may not lead to stenosis and/or occlusion of the intracranial large arteries but may promote pathological angiogenesis in the small arteries. Previous studies have shown that these abnormally proliferative small arteries contain an incomplete vascular structure and that the development of moyamoya vessels occurs ahead of regional stenosis and/or occlusion.[43,44] A clinical follow-up study with MRA has also revealed that the reappearance of moyamoya vessels is independent of previously steno-occlusive arteries in MMD patients who are undergoing surgical revascularization.[45] Although moyamoya vessels are viewed as evidence of a physiological compensatory mechanism to supplement regional blood flow, our findings suggest that the proliferative vasculopathy caused by *RNF213* mutations in MMD is a typical feature.

Endothelial knockout of the *RNF213* gene has been found to damage cell–cell junctions and promote endothelial cell migration by activating inflammatory pathways in a cell culture model *in vitro*.[46] Overexpression of *RNF213* significantly inhibits tube formation by suppressing the PI3K-Akt signalling pathway.[47,48] Furthermore, our study confirmed that HBMECs were the major sources of non-secreted RNF213 protein, and knockdown of *RNF213* expression significantly increased endothelial cell proliferation, migration and tube formation *in vitro*. However, these abilities were markedly enhanced early in the experimental treatment period, and the effect of *RNF213* knockdown gradually weakened over time. Indeed, the long-term cumulative effects of *RNF213* mutations should be explored in the future.

We next sought to obtain a more comprehensive mechanistic understanding of the relationship between loss-of-function of *RNF213* and moyamoya vessels. Our data showed that endothelial *RNF213* knockdown activated the Hippo pathway effector *YAP/TAZ* and induced the expression of the downstream effector *VEGFR2* (Fig. 8). Inhibition of *YAP/TAZ* resulted in an altered cellular distribution of *VEGFR2* due to defects in trafficking from the Golgi apparatus to the plasma membrane and reversed *RNF213* knockdown-induced angiogenesis.

Furthermore, the *VEGF-VEGFR2* axis induced vascular remodelling by regulating the *SCR* kinase family and cytoskeleton, but its effects were constrained by YAP/TAZ protein activity.[32,34] Upregulated *YAP/TAZ* expression promoted VEGFR2 protein expression, and the *VEGF-VEGFR2* axis suppressed *MST1/2* and *LAST1/2* through a feedback loop.[49] Our data also revealed that *YAP/TAZ* levels were positively correlated with angiogenesis. Compared with YAP/TAZ inhibitor treatment, *YAP/TAZ* knockdown in HBMECs only slightly reduced *VEGFR2* expression. In this study, we tried to rectify the reduction in *RNF213* expression through plasmid DNA transfection. Supplementation with a small amount of *RNF213* led to a decrease in *YAP/TAZ* mRNA expression, but overexpression of *RNF213* by more than 12-fold led to a significant increase in *YAP/TAZ* expression, indicating that strongly elevated *RNF213* expression led to dysfunction of this negative feedback loop. Moreover, Hippo signalling reciprocally promoted Notch signalling while antagonizing NF-κB and Wnt/β-catenin signalling.[50–52] Thus, *RNF213* knockdown-induced MMD pathogenesis involves pathways in addition to the Hippo signalling pathway, and more molecular networks should be explored in the future.

This study had a few limitations. First, we identified a novel *RNF213* mutation in several patients with sporadic MMD, but we

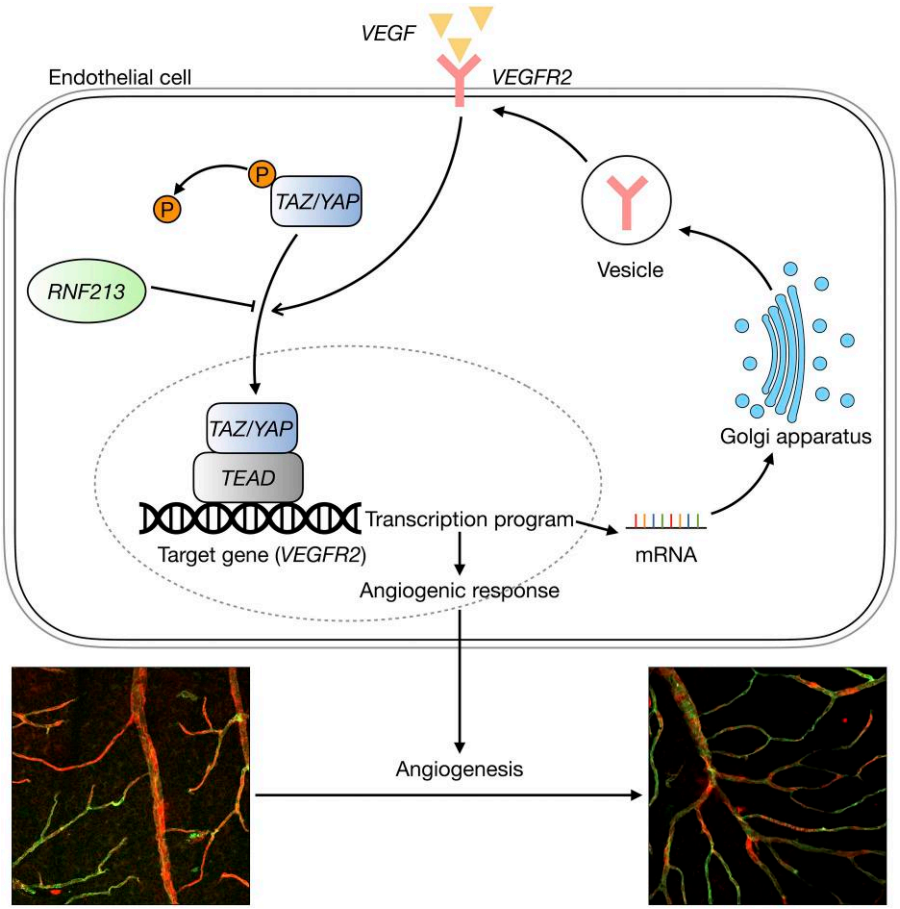

Figure 8 Schematic showing the mechanism by which *RNF213* loss-of-function mutations regulate the Hippo signalling pathway in endothelial cells. Green = IB-4; red = *α-SMA*.

did not test their parents. The heterozygous mutation cannot be concluded to be inherited. Because the evidence supporting it as a loss-of-function mutation is not sufficiently strong (lack of validation in a large sample), all experiments using human samples were conducted on STA samples from MMD patients carrying the pathogenic p.R4810K mutation. In addition, we observed an increased number of endothelial cells from *RNF213*-deficient animals by labelling vessel markers, but the effects of veins could not be excluded. Moreover, p-VEGFR2 is the active component and starting factor initiating downstream signalling pathways in angiogenesis. However, the level of the VEGFR2 protein phosphorylated at different sites varied substantially in *siRNF213*-treated HBMECs. Owing to a cross-reaction with VEGFR1 and VEGFR3 (which have protein weights similar to that of the p-VEGFR2 antibody), changes in these confounding proteins might have influenced the actual p-VEGFR2 concentration. Because the targeted tyrosine sites of *VEGFR2* were not fully discovered, variations in the phosphorylation of several sites were not sufficiently accurate to confirm *VEGFR2* activation. Although our study identified a significant increase in membrane *VEGFR2* levels in endothelial cells, this finding must be validated in the future. Finally, the increased mRNA expression of *YAP/TAZ* in *siRNF213*-treated HBMECs could not be explained by low ubiquitination activity, but YAP/TAZ protein stability is controlled by an appropriate balance between E3 ubiquitin ligases and deubiquitinases. Since loss-of-function of *RNF213* disrupted the K63-linked polyubiquitin chains,[53] we hypothesized that endothelial *RNF213* knockdown could stabilize and activate *YAP/TAZ* via hypo-ubiquitination to a certain extent; this hypothesis should be tested in further studies.

Taken together, our results reveal that *RNF213* knockdown mediates *VEGFR2* overexpression by activating the Hippo pathway effector *YAP/TAZ* during pathological angiogenesis. Inhibition of *YAP/TAZ* expression might represent a therapeutic target for MMD patients with *RNF213* loss-of-function.

Data availability

The authors declare that all supporting data are available within the article, the Supplementary material, and the National Genomics Data Center (https://ngdc.cncb.ac.cn/, accession numbers: HRA002920 and HRA002922).

Acknowledgements

We thank Hua Feng (Department of Neurosurgery, Southwest Hospital, Army Medical University) for the study design and technical guidance, Wenjuan Wan (Department of Ophthalmology, The First Affiliated Hospital of Chongqing Medical University) for assistance with whole-mount immunofluorescence staining of mouse retinas, and Wenting Jiang (Institute of Precision Medicine, The First Affiliated Hospital, Sun Yat-sen University) for assistance with flow cytometry and the confocal imaging system. We thank the Beijing

Genomics Institute (Shenzhen, CHN) for data processing and analysis of the whole-genome sequencing and Sanger sequencing data and the Applied Protein Technology Biotech Company (Shanghai, CHN) for processing and analysing the RNA sequencing data.

Funding

This work was funded by the National Natural Science Foundation of China (82071286, 81671132, and 81471180) and the National Natural Science Foundation of Chongqing, China (CSTB2023NSCQ-BHX0204).

Competing interests

The authors report no competing interests.

Supplementary material

Supplementary material is available at *Brain* online.

References

1. Scott RM, Smith ER. Moyamoya disease and moyamoya syndrome. *N Engl J Med*. 2009;360:1226-1237.
2. Kim JS. Moyamoya disease: Epidemiology, clinical features, and diagnosis. *J Stroke*. 2016;18:2-11.
3. Baba T, Houkin K, Kuroda S. Novel epidemiological features of moyamoya disease. *J Neurol Neurosurg Psychiatry*. 2008;79:900-904.
4. Takagi Y, Kikuta K, Nozaki K, Hashimoto N. Histological features of middle cerebral arteries from patients treated for moyamoya disease. *Neurol Med Chir (Tokyo)*. 2007;47:1-4.
5. Research Committee on the Pathology and Treatment of Spontaneous Occlusion of the Circle of Willis; Health Labour Sciences Research Grant for Research on Measures for Infractable Diseases. Guidelines for diagnosis and treatment of moyamoya disease (spontaneous occlusion of the circle of willis). *Neurol Med Chir (Tokyo)*. 2012;52:245-266.
6. Fujimura M, Tominaga T. Diagnosis of moyamoya disease: International standard and regional differences. *Neurol Med Chir (Tokyo)*. 2015;55:189-193.
7. Fujimura M, Sonobe S, Nishijima Y, *et al*. Genetics and biomarkers of moyamoya disease: Significance of RNF213 as a susceptibility gene. *J Stroke*. 2014;16:65-72.
8. Kim T, Oh CW, Bang JS, Kim JE, Cho WS. Moyamoya disease: Treatment and outcomes. *J Stroke*. 2016;18:21-30.
9. Liu W, Morito D, Takashima S, *et al*. Identification of RNF213 as a susceptibility gene for moyamoya disease and its possible role in vascular development. *PLoS One*. 2011;6:e22542.
10. Duan L, Wei L, Tian Y, *et al*. Novel susceptibility loci for moyamoya disease revealed by a genome-wide association study. *Stroke*. 2018;49:11-18.
11. Gagunashvili AN, Ocaka L, Kelberman D, *et al*. Novel missense variants in the RNF213 gene from a European family with moyamoya disease. *Hum Genome Var*. 2019;6:35.
12. Miyatake S, Touho H, Miyake N, *et al*. Sibling cases of moyamoya disease having homozygous and heterozygous c.14576G > A variant in RNF213 showed varying clinical course and severity. *J Hum Genet*. 2012;57:804-806.
13. Miyatake S, Miyake N, Touho H, *et al*. Homozygous c.14576G > A variant of RNF213 predicts early-onset and severe form of moyamoya disease. *Neurology*. 2012;78:803-810.
14. Kamada F, Aoki Y, Narisawa A, *et al*. A genome-wide association study identifies RNF213 as the first moyamoya disease gene. *J Hum Genet*. 2011;56:34-40.
15. Cecchi AC, Guo D, Ren Z, *et al*. RNF213 Rare variants in an ethnically diverse population with moyamoya disease. *Stroke*. 2014;45:3200-3207.
16. Ahel J, Lehner A, Vogel A, *et al*. Moyamoya disease factor RNF213 is a giant E3 ligase with a dynein-like core and a distinct ubiquitin-transfer mechanism. *Elife*. 2020;9:e56185.
17. Pinard A, Fiander MDJ, Cecchi AC, *et al*. Association of De Novo *RNF213* variants with childhood onset moyamoya disease and diffuse occlusive vasculopathy. *Neurology*. 2021;96:e1783-e1791.
18. Hanemaaijer NM, Sikkema-Raddatz B, van der Vries G, *et al*. Practical guidelines for interpreting copy number gains detected by high-resolution array in routine diagnostics. *Eur J Hum Genet*. 2012;20:161-165.
19. Bhardwaj A, Banh RS, Zhang W, Sidhu SS, Neel BG. MMD-associated *RNF213* SNPs encode dominant-negative alleles that globally impair ubiquitylation. *Life Sci Alliance*. 2022;5:e202000807.
20. Ihara M, Yamamoto Y, Hattori Y, *et al*. Moyamoya disease: Diagnosis and interventions. *Lancet Neurol*. 2022;21:747-758.
21. Falk E. Pathogenesis of atherosclerosis. *J Am Coll Cardiol*. 2006;47:C7-C12.
22. Sonobe S, Fujimura M, Niizuma K, *et al*. Temporal profile of the vascular anatomy evaluated by 9.4-T magnetic resonance angiography and histopathological analysis in mice lacking RNF213: A susceptibility gene for moyamoya disease. *Brain Res*. 2014;1552:64-71.
23. Kanoke A, Fujimura M, Niizuma K, *et al*. Temporal profile of the vascular anatomy evaluated by 9.4-tesla magnetic resonance angiography and histological analysis in mice with the R4859K mutation of RNF213, the susceptibility gene for moyamoya disease. *Brain Res*. 2015;1624:497-505.
24. Zudaire E, Gambardella L, Kurcz C, Vermeren S. A computational tool for quantitative analysis of vascular networks. *PLoS One*. 2011;6:e27385.
25. Wen J, Sun X, Chen H, *et al*. Mutation of rnf213a by TALEN causes abnormal angiogenesis and circulation defects in zebrafish. *Brain Res*. 2016;1644:70-78.
26. Lin J, Liang J, Wen J, *et al*. Mutations of *RNF213* are responsible for sporadic cerebral cavernous malformation and lead to a mulberry-like cluster in zebrafish. *J Cereb Blood Flow Metab*. 2021;41:1251-1263.
27. Ito A, Fujimura M, Niizuma K, *et al*. Enhanced postischaemic angiogenesis in mice lacking RNF213; a susceptibility gene for moyamoya disease. *Brain Res*. 2015;1594:310-320.
28. Zhou G, Soufan O, Ewald J, Hancock REW, Basu N, Xia J. Networkanalyst 3.0: A visual analytics platform for comprehensive gene expression profiling and meta-analysis. *Nucleic Acids Res*. 2019;47:W234-W241.
29. Sherman BT, Hao M, Qiu J, *et al*. DAVID: A web server for functional enrichment analysis and functional annotation of gene lists (2021 update). *Nucleic Acids Res*. 2022;50:W216–W221.
30. Gene Ontology Consortium. Gene ontology consortium: Going forward. *Nucleic Acids Res*. 2015;43:D1049-D1056.
31. Kanehisa M, Furumichi M, Tanabe M, Sato Y, Morishima K. KEGG: New perspectives on genomes, pathways, diseases and drugs. *Nucleic Acids Res*. 2017;45:D353-D361.
32. Kim J, Kim YH, Kim J, *et al*. YAP/TAZ regulates sprouting angiogenesis and vascular barrier maturation. *J Clin Invest*. 2017;127:3441-3461.
33. Moya IM, Halder G. Hippo-YAP/TAZ signalling in organ regeneration and regenerative medicine. *Nat Rev Mol Cell Biol*. 2019;20:211-226.

34. Wang X, Freire Valls A, Schermann G, *et al*. YAP/TAZ orchestrate VEGF signalling during developmental angiogenesis. *Dev Cell*. 2017;42:462-478.
35. Tokairin K, Hamauchi S, Ito M, *et al*. Vascular smooth muscle cell derived from IPS cell of moyamoya disease - comparative characterization with endothelial cell transcriptome. *J Stroke Cerebrovasc Dis*. 2020;29:105305.
36. Phi JH, Suzuki N, Moon YJ, *et al*. Chemokine ligand 5 (CCL5) derived from endothelial colony-forming cells (ECFCs) mediates recruitment of smooth muscle progenitor cells (SPCs) toward critical vascular locations in moyamoya disease. *PLoS One*. 2017;12:e0169714.
37. Kotani Y, Morito D, Yamazaki S, *et al*. Neuromuscular regulation in zebrafish by a large AAA+ ATPase/ubiquitin ligase, mysterin/RNF213. *Sci Rep*. 2015;5:16161.
38. Guo DC, Papke CL, Tran-Fadulu V, *et al*. Mutations in smooth muscle alpha-actin (ACTA2) cause coronary artery disease, stroke, and moyamoya disease, along with thoracic aortic disease. *Am J Hum Genet*. 2009; 84:617-627.
39. Liu Y, Huang Y, Zhang X, *et al*. CircZXDC promotes vascular smooth muscle cell transdifferentiation via regulating miRNA-125a-3p/ABCC6 in moyamoya disease. *Cells*. 2022; 11:3792.
40. Otten EG, Werner E, Crespillo-Casado A, *et al*. Ubiquitylation of lipopolysaccharide by RNF213 during bacterial infection. *Nature*. 2021;594:111-116.
41. Louvrier C, Awad F, Cosnes A, *et al*. RNF213-associated Urticarial lesions with hypercytokinemia. *J Allergy Clin Immunol*. 2022;150: 1545-1555.
42. Imani SZH, Hojati Z, Khalilian S, *et al*. Expression and clinical significance of IL7R, NFATc2, and RNF213 in familial and sporadic multiple sclerosis. *Sci Rep*. 2021;11: 19260.
43. Bang OY, Fujimura M, Kim SK. The pathophysiology of moyamoya disease: An update. *J Stroke*. 2016;18:12-20.
44. Kim SJ, Son TO, Kim KH, *et al*. Neovascularization precedes occlusion in moyamoya disease: Angiographic findings in 172 paediatric patients. *Eur Neurol*. 2014;72:299-305.
45. Houkin K, Nakayama N, Kuroda S, Ishikawa T, Nonaka T. How does angiogenesis develop in paediatric moyamoya disease after surgery? A prospective study with MR angiography. *Childs Nerv Syst*. 2004;20:734-741.
46. Roy V, Ross JP, Pépin R, *et al*. Moyamoya disease susceptibility gene *RNF213*Regulates endothelial barrier function. *Stroke*. 2022;53:1263-1275.
47. Hitomi T, Habu T, Kobayashi H, *et al*. Downregulation of securin by the variant RNF213 R4810K (rs112735431, G > A) reduces angiogenic activity of induced pluripotent stem cell-derived vascular endothelial cells from moyamoya patients. *Biochem Biophys Res Commun*. 2013;438:13-19.
48. Ohkubo K, Sakai Y, Inoue H, *et al*. Moyamoya disease susceptibility gene RNF213 links inflammatory and angiogenic signals in endothelial cells. *Sci Rep*. 2015;5:13191.
49. Azad T, Janse van Rensburg HJ, Lightbody ED, *et al*. A LATS biosensor screen identifies VEGFR as a regulator of the hippo pathway in angiogenesis. *Nat Commun*. 2018;9:1061.
50. Deng Y, Lu J, Li W, *et al*. Reciprocal inhibition of YAP/TAZ and NF-κB regulates osteoarthritic cartilage degradation. *Nat Commun*. 2018;9:4564.
51. Kim W, Khan SK, Gvozdenovic-Jeremic J, *et al*. Hippo signalling interactions with wnt/β-catenin and notch signalling repress liver tumorigenesis. *J Clin Invest*. 2017;127:137-152.
52. Heallen T, Zhang M, Wang J, *et al*. Hippo pathway inhibits wnt signalling to restrain cardiomyocyte proliferation and heart size. *Science*. 2011;332:458-461.
53. Takeda M, Tezuka T, Kim M, *et al*. Moyamoya disease patient mutations in the RING domain of RNF213 reduce its ubiquitin ligase activity and enhance NFκB activation and apoptosis in an AAA+ domain-dependent manner. *Biochem Biophys Res Commun*. 2020;525:668-674.